U. Walzer and R. Hendel. Mantle convection and evolution with growing continents.
J. Geophys. Res., 113, B09405, doi: 10.1029/2007JB005459, 2008.

Mantle convection and evolution with growing continents

Uwe Walzer[1] and Roland Hendel[1]

Received 22 October 2007; revised 1 April 2008; accepted 6 May 2008; published 10 September 2008.

[1] We present a three-dimensional spherical shell numerical model for chemical differentiation and redistribution of incompatible elements in a convective Earth's mantle heated mostly from within by U, Th, and K and slightly from below. The evolution-model equations guarantee conservation of mass, momentum, energy, angular momentum, and four sums of the number of atoms of the pairs $^{238}U-^{206}Pb$, $^{235}U-^{207}Pb$, $^{232}Th-^{208}Pb$, and $^{40}K-^{40}Ar$. The pressure- and temperature-dependent viscosity is supplemented by a viscoplastic yield stress, σ_y. The lithospheric viscosity is partly imposed to mimic its increase by dehydration of oceanic lithosphere and other effects. Also, the asthenosphere is generated not only by the distribution of temperature and melting temperature, but essentially by the profiles of water solubility and water abundance. Therefore we introduced a radial viscosity profile factor describing that behavior. However, the focus of this paper is the episodic growth of continents and oceanic plateaus. As a complement, the differentiation generates the depleted MORB mantle (DMM) which predominates immediately beneath the lithosphere. Our continents are not artificially imposed on the surface of the spherical shell, but instead they evolve by the interplay between chemical differentiation and convection/mixing. No restrictions are imposed regarding number, size, form, and distribution of continents. However, oceanic plateaus that impinge upon a continent have to be united with it. This mimics the accretion of terranes. The numerical results show an episodic growth of the total mass of the continents and display a plausible time history for the laterally averaged surface heat flow, *qob*, and the Rayleigh number, *Ra*. We use our model to explore a moderate region of $Ra-\sigma_y$ parameter space. We find Earth-like continent distributions in a central part of the $Ra-\sigma_y$ space we explored. We identified a $Ra-\sigma_y$ region where the calculated total continental volume is very close to the observed value; another $Ra-\sigma_y$ region where the Urey number, *Ur*, is close to the accepted value; a third $Ra-\sigma_y$ area where surface heat flow is very close to the present-day observed mean global heat flow using typical abundances of the heat-producing elements. It is remarkable that these different acceptable $Ra-\sigma_y$ regions share a common overlap area, where Earth-like behavior is simultaneously fulfilled.Although the convective flow patterns and the chemical differentiation of oceanic plateaus are coupled, the evolution of time-dependent Rayleigh number, Ra_t, is relatively well predictable and the stochastic parts of the $Ra_t(t)$ curves are small. Regarding the time distribution of juvenile growth rates of the total mass of the continents, predictions are possible only in the first epoch of the evolution, presumed that the initial conditions are given. Later on, the distribution of the continental growth episodes is increasingly stochastic. Independent of the varying individual runs, our model shows that the total mass of the present-day continents is not generated in a single process at the beginning of the thermal evolution of the Earth but in episodically distributed processes. This is in accord with observation.

Citation: Walzer, U., and R. Hendel (2008), Mantle convection and evolution with growing continents, *J. Geophys. Res.*, *113*, B09405, doi:10.1029/2007JB005459.

1. Introduction

[2] *Schubert et al.* [2001] review the may lines of evidence why solid state convection explains the thermal evolution of the Earth's mantle. *Ogawa* [2008] presents an outline of thermochemical convection in the mantle, its relation to superplumes, chemical differentiation and plate tectonic activities. The focus of our paper is a three-dimensional spherical shell convection model with dynamically evolving continents which grow episodically. Both continents and lithospheric partial shells of the model move plate-like with piecewise different rotation velocities around the Earth's center where the plate boundaries freely evolve

[1]Institut f. Geowissenschaften, Friedrich-Schiller-Universität, Burgweg, Jena, Germany.

as a function of time. Finally, we vary the Rayleigh number, Ra, and the viscoplastic yield stress, σ_y, to determine the boundaries of the realistic regime in the $Ra-\sigma_y$ space. This introduction is divided into four subsections since our model contributes to different partial fields.

1.1. Generation and Episodic Growth of Continents: Observations

[3] The problem of the development of continents is very complex [*Windley*, 1995; *Fei et al.*, 1999; *van der Hilst and McDonough*, 1999; *Fowler et al.*, 2002; *Jones et al.*, 2004; *Sleep*, 2005; *Hawkesworth and Kemp*, 2006; *Brown and Rushmer*, 2006]. The timing of generation of continents has been debated by *Taylor and McLennan* [1995] and *Bowring and Housh* [1995]. *Condie* [2000] and *Kemp et al.* [2006] show that the total volume of continents did *not* originate as a whole at the beginning of the Earth's thermal evolution but by repeated differentiation cycles. Only about one half of the present total volume was produced by chemical differentiation until the end of the Archean, 2500 Ma ago. *Kramers and Tolstikhin* [1997] conclude from the U–Th–Pb isotope system, *Nagler and Kramers* [1998] deduce from the neodymium system that less than 10% of the present mass of the continental crust have existed 4400 Ma ago. *Fisher and Schmincke* [1984] estimate that today about 62 vol.% of the general crustal growth takes place at divergent plate boundaries, about 24 vol. % at convergent plate boundaries and only about 12 vol. % as ocean island and plateau basalts by plumes. The differentiation of continental material via oceanic plateaus complementary creates a depleted part of the mantle beneath the lithosphere. Observational evidence suggests that the contribution of oceanic plateaus to continental growth seems to have been considerably larger than that of the midocean ridge basalt (MORB) of the divergent plate boundaries in the bulk of earlier geological epochs compared to the present [*Parman*, 2007]. In epochs of heavy continental growth, the contribution of plateau basalts were considerably larger than today, and these mantle-differentiation events had an episodic temporal distribution [*Coffin and Eldholm*, 1994]. There are clearly investigated examples of large oceanic plateaus which have been accreted to the Americas [*Howell*, 1989; *Arculus et al.*, 1999]. *Abbott et al.* [1997] and *Albarède* [1998] concluded that the accretion of oceanic plateau basalts to the continental crust (CC) is, considering the whole time span of Earth's history, the dominant process and that basaltic crust with more than 25 km thickness cannot be subducted. However, there are also some other mechanisms which contribute to continental growth [*Davidson and Arculus*, 2006]. Our present numerical model of the dynamics of continental growth is based on geochemical observations and its generalization given by *Hofmann* [1988, 2003]. Incompatible elements have large s, p, d, and f radii. Therefore these elements do not fit well into the silicate lattices of the mantle and Rb, Pb, U, Th, K, La etc. are enriched in partial melts. These melts rise and form the oceanic plateaus leaving behind the depleted MORB mantle (DMM). So DMM is depleted in comparison to the primitive mantle (PM). In this way, three reservoirs (CC, DMM, PM) of the silicate shell of the Earth are generated. They have different abundances of the dominating heat-producing elements, U, Th, and K, that drive the solid-state convection mainly by heating from within. The further chemical differentiation of DMM at the midoceanic ridges into a basaltic oceanic crust and the harzburgitic and lherzolitic layers of the oceanic lithospheric mantle has been taken into account only regarding its effect on lithospheric viscosity.

1.2. Mantle Convection With Continents

[4] Most of numerical mantle convection models do not contain continents at all but consider other problems. Models with continents mainly investigate the effects of continents on mantle dynamics where the continents are imposed. *Gurnis* [1988] and *Zhong and Gurnis* [1993] study the dynamic feedback between the motions of the imposed continental plates and mantle convection in a two-dimensional model. They conclude that the continental velocity is intrinsically episodic. Using a two-dimensional convection model with aspect ratio 24, *Lowman and Jarvis* [1996] observe a collision of imposed continents and the subsequent reorganization of the convective planforms into a smaller wavelength mode which breaks apart the continents. The two-dimensional model of *Lenardic et al.* [2005], however, leads to a somewhat nonintuitive result, namely that imposed continents, acting as thermal insulators on top of a convecting two-dimensional mantle, can enhance mantle cooling.

[5] Three-dimensional spherical shell mantle convection models with imposed continents have been presented by *Phillips and Bunge* [2005] and *Zhong et al.* [2007]. *Phillips and Bunge* [2005] imposed semispherical caps of 30%, 10%, and 3% of Earth's surface with small circle borders. These continental caps are constructed in such a way that the mean heat flux through the continent is about half that through the ocean bottom. Smaller continents are, as expected, unable to promote long-wavelength structures and show velocity maxima after each 100 million years or so. *Zhong et al.* [2007] included a radially variable viscosity but either no continent or only one supercontinent. In the three-dimensional spherical shell model of our paper, the continents are not imposed. They evolve by a simplified chemical differentiation as a function of time. Their number or sizes are not prescribed.

1.3. Plate-Like Motions of the Lithosphere

[6] The usual explanation of plate-like behavior of continents is chemical buoyancy and high viscosity. *Lenardic et al.* [2003] are of the opinion that, furthermore, the relatively high brittle yield stress plays a role. It is more difficult to explain the plate-like motion and subduction of the oceanic lithosphere which is the surface expression of mantle convection.

[7] Already early it has been assumed that the extremely strong temperature dependence of the viscosity is the cause of the high strength of the oceanic lithosphere. Many numerical experiments with strong temperature dependence of the viscosity have been performed to study various mantle-relevant problems [*Christensen*, 1984, 1985a; *Ogawa et al.*, 1991; *Christensen and Harder*, 1991; *Tackley*, 1993; *Hansen and Yuen*, 1993; *Moresi and Solomatov*, 1995; *Kameyama and Ogawa*, 2000]. It has been proven

accepted for publication in JOURNAL OF GEOPHYSICAL RESEARCH , 6 May 2008

that it is not possible to produce plate tectonic behavior by a purely viscous rheology and without asthenosphere. *Solomatov* [1995] and *Kameyama and Ogawa* [2000] showed that there are three different regime regions in a plot with the axes Rayleigh number and viscosity contrast between top and bottom boundaries: stagnant-lid regime, sluggish-lid regime and small viscosity contrast regime. The sluggish-lid regime shows a certain similarity to the oceanic lithosphere but, in the model, the deformation is distributed over the whole lithosphere. On the Earth, however, the plate interiors are almost rigid and the deformation is mainly concentrated near the plate boundaries. Different models generate plate-like behavior in rather different ways. *Hager and O'Connell* [1981] and *Bunge and Richards* [1996] imposed the velocity field at the surface. As opposed to this, *Gable et al.* [1991] and *Monnereau and Quéré* [2001] prescribed only the initial plate geometry and introduced a coupling between plates and bulk convection supposing no direct interaction between the plates. There is a certain free space between the plates to allow an evolution of the plates. In this way, they avoid the numerical treatment of a complex rheology that deviates from the Newtonian case.

[8] However, a primary goal of mantle convection investigation has been to find self-consistent solutions to the plate-generation problem. Both pure Newtonian rheology and pure power law non-Newtonian rheology proved to be inadequate to give a self-consistent solution. Therefore the Newtonian creep has been supplemented by different mechanisms, e.g., viscoplastic yield stress, strain weakening, self-lubrication, grain-size-dependent rheologies and damage mechanisms [*Bercovici*, 1996, 1998, 2003; *Trompert and Hansen*, 1998; *Tackley*, 2000a, 2000b]. *Trompert and Hansen* [1998] found episodic self-consistent plate-like behavior in a three-dimensional box model, interrupted by periods with a stagnant lid. *Stein et al.* [2004] added the pressure dependence of viscosity and of thermal expansivity to such a model and found continuous plate motion and the appearance of an asthenosphere. *Tackley* [2000b] has also investigated the influence of pressure dependence of viscosity on plate motion. The reduction in mineral grain size in shear zones could also be an important mechanism for shear localization in the upper layers of the oceanic lithosphere. At present, many of these issues cannot be sufficiently numerically represented in the models since the grid is too coarse yet. It is well-known from the geology of continents that mechanically weak zones store the "knowledge" of formerly active faults and that the lithosphere tends to break again at these locations. Therefore *Ogawa* [2003a] introduced a damage parameter into the viscosity relation. Although the generation of plate-like behavior is not the main subject of this paper, we present our preliminary solution of the problem in section 3.1.

1.4. Chemical Differentiation

[9] Chemical differentiation alters the distribution of radioactive elements and volatiles and generates geochemical heterogeneity. On the other hand, convective stirring diminishes and annihilates these chemical heterogeneities. This paper seeks to account for both differentiation and convection/mixing together. The focus, however, is the evolution of continents and oceanic plateaus and, as a complement, of the MORB source [*Hofmann*, 1988, 2003]. *Tackley* [2000c] has provided an overview of the interaction between mantle convection and generation of chemical heterogeneity. Earlier, *Ogawa* [1993, 1994] described a two-dimensional thermochemical convection model of a binary eutectic material $A_\xi B_{1-\xi}$ where A is harzburgite and B is a mixture of clinopyroxene and garnet. The eutectic distribution $A_{0.1}B_{0.9}$ corresponds to basaltic composition. *Ogawa* [2003b] assumed that the primitive material ($A_{0.64}B_{0.36}$) had a smaller reference density, smaller than that of the basaltic material. In the *Ogawa* [1993, 1994] model, two layers with a chemical discontinuity, not only of the heat-producing elements, but also of the major elements arise: The lower layer is mainly a dense, low-ξ magmatic product, while the upper layer is a less dense high-ξ material. Layered convection is observed for some interval of time. However, later in the model calculation, this structure is catastrophically destroyed leading to a more chemically homogeneous mantle. Depending on the viscosity assumptions, the destruction of the chemically layered structure can occur in the early Earth, at a later date, or even yet in the future.

[10] Other models by *Christensen and Hofmann* [1994], *Sidorin and Gurnis* [1998], and *Davies* [2002] yield considerably thinner layers that are different from the main part of the mantle with respect to major element distribution and correspond to the D″ layer that develops from subducted oceanic crust. *Davies*' [2006] results show only a very thin dense layer at the base of the mantle. *Ogawa* [1997] studied the convection of a binary eutectic material of constant viscosity in a two-dimensional box. He found the state of the system had two branches: chemically stratified structure arose in the upper mantle during the Archean and the early Proterozoic, and an unstratified whole mantle convection branch began at the end of the early Proterozoic. *Ogawa* [2000] improved his square Cartesian box model by adding temperature- and pressure-dependent viscosity as well as the phase transformation at 660 km depth. This model displayed layered convection with episodic flushing events. However, the chemical discontinuity remained stable for billions of years. He discussed the influence of different values for the negative Clausius–Clapeyron slope on the results. *Kameyama and Ogawa* [2000] then applied that model to a wide box. In the *Ogawa* [2003b] models, chemical stratification develops regardless of the strength of the olivine barrier and lithospheric plates move if the mass exchange through the 660-km discontinuity is not strongly impeded by the olivine barrier. Despite these advances in numerical modeling, there is currently no consensus regarding the present-day spatial distribution of chemically distinct reservoirs in the Earth's mantle, where the main point for our present model is the abundance distribution of heat-producing elements. However, the following consideration seems to be rather evident.

[11] The present-day heat output of the mantle is 36 TW and it is not possible to produce such a large amount of heat from a mantle of DMM composition [*Bercovici and Karato*, 2003]. A more detailed reasoning is as follows: The Earth's present-day heat loss is 44 TW [*Pollak et al.*, 1993]. 4.8–9.6 TW of it are produced by the Continental Crust (CC) [*Taylor and McLennan*, 1985; *Rudnick and Fountain*, 1995; *Porcelli and Ballentine*, 2002]. The different numbers stem from

accepted for publication in JOURNAL OF GEOPHYSICAL RESEARCH , 6 May 2008

different assumptions on the average CC abundances of radioactive elements. The contribution of the Earth's core is between 3 and 7 TW [*Buffett et al.*, 1996]. Assuming the DMM abundances are a factor 1/2.6 smaller than the Bulk Silicate Earth (BSE) abundances according to *Jochum et al.* [1983], then a whole mantle DMM would generate only 7.2 TW [*Porcelli and Ballentine*, 2002]. The contribution of secular cooling is between 21.8 TW and 17.8 TW. If the contributions of the CC, the core, and secular cooling are subtracted from the observed 44 TW, then between 9.6 and 14.4 TW must be generated in the mantle. However, these values exceed the 7.2 TW of a hypothetical mantle comprised entirely of DMM. Therefore the mantle must contain at least one reservoir that is enriched in heat producing elements.

[12] In the meantime, the theory of geochemical reservoirs has been further refined [*Hofmann*, 2003; *Bennett*, 2003] such that the reservoirs are no longer necessarily understood as separate large-scale volumes. For example, *Stracke et al.* [2005] and *Willbold and Stracke* [2006] propose a new FOZO similar to the traditional FOZO except that this new FOZO is a small-scale component, ubiquitously dispersed throughout the entire mantle. The exact definition of FOZO can be found in *Hart et al.* [1992]. A short definition would be as follows. When the isotope ratio of a single element is plotted against the isotope ratio of another element, for many basaltic rocks from around the world, including IOBs and MORBs, they tend to scatter into mixing lines. If all mixing arrays are plotted, e.g. in a three-dimensional $^{206}Pb-^{204}Pb$, $^{87}Sr-^{86}Sr$, $^{143}Nd-^{144}Nd$ diagram then all mixing lines aim at a small volume called focal zone or FOZO. However, in most current reservoir models, the percentages of the reservoirs can systematically vary across the mantle. We remark that, according to the results of our present dynamic model, the percentage of FOZO in the uppermost part of the mantle should be less than in the lower mantle. Furthermore, we obtain the result that the mantle immediately beneath the lithosphere is nearly exclusively DMM. Using the conception of current reservoir models, the mantle is everywhere heterogeneous and only the mixing ratios of the reservoirs vary. Whether or not such a distributed geochemical reservoir theory is viable is still an open issue.

2. Model Description

[13] This paper is in essence a numerical study of three-dimensional solid-state mantle convection in a spherical shell with growing continents. It is neither technically possible nor scientifically appropriate to include all known geophysical and geochemical aspects of the mantle evolution problem. Thus, for example, the model does not include the very early epoch of magma ocean since our treatment is restricted to solid-state creep. Further, we restrict chemical differentiation mainly to the incompatible elements that heavily influence internal heating and buoyancy. However, our continents are not artificially imposed but instead evolve by chemical differentiation as described below. Neither their number nor their form, or size or position are prescribed. These aspects of our treatment of continents are determined exclusively by the interplay between convection/mixing and differentiation. We developed the model step by step. Section 3.1 presents some physical results of a preliminary version without continent differentiation.

2.1. Balance Equations

[14] We solve the differential equations of infinite Prandtl number convection within a three-dimensional spherical shell using a finite element method. We adopt the inelastic liquid approximation to obtain our equation for mass balance.

$$\nabla \cdot \mathbf{v} = -\frac{1}{\rho}\mathbf{v} \cdot \nabla\rho \tag{1}$$

where ρ is density, and $\mathbf{v}$ is velocity. For energy balance we use the equation

$$\frac{\partial T}{\partial t} = -\frac{\partial (T v_j)}{\partial x_j} - (\gamma - 1) T \frac{\partial v_j}{\partial x_j} + \frac{1}{\rho c_v}\left[\tau_{ik}\frac{\partial v_i}{\partial x_k} + \frac{\partial}{\partial x_j}\left(k\frac{\partial}{\partial x_j}T\right) + Q\right] \tag{2}$$

where T signifies temperature, t time, v_j velocity, x_j position, γ Grüneisen parameter, c_v specific heat at constant volume, τ_{ik} deviatoric stress, k thermal conductivity and Q heat generation rate per unit volume. Q is a function of position and time because of the chemical differentiation the numerical approximation of which is outlined in section 2.4 and Appendix A. The deviatoric stress tensor, τ_{ik}, is given by

$$\tau_{ik} = \eta\left(\frac{\partial v_i}{\partial x_k} + \frac{\partial v_k}{\partial x_i} - \frac{2}{3}\frac{\partial v_j}{\partial x_j}\delta_{ik}\right) \tag{3}$$

where η denotes the viscosity. Although c_v appears in equation (2), this expression is exactly equivalent to the well-known energy conservation equation in which c_p is used. Equation (2) is advantageous since the Grüneisen gamma of the Earth's mantle can be derived from PREM [*Dziewonski and Anderson*, 1981] or other models based on seismic observations via the formula of the *Vashchenko and Zubarev* [1963] gamma.

[15] As our equation of state we take

$$\rho = \rho_r\left[1 - \alpha(T - T_r) + \frac{(P - P_r)}{K_T} + \sum_{k=1}^{2}\Gamma_k\frac{\Delta\rho_k}{\rho_r}\right] \tag{4}$$

where α is the coefficient of thermal expansion, K_T isothermal bulk modulus and P pressure. The index r refers to the adiabatic reference state and $\Delta\rho_k/\rho_r$ or f_{ak} denotes the nondimensional density jump for the kth mineral phase transition. Γ_k is a measure of the relative fraction of the heavier phase where $\Gamma_k = \frac{1}{2}\left(1 + \tanh\frac{\pi_k}{d_k}\right)$ with $\pi_k = P - P_{0k} - \gamma_k T$ describing the excess pressure, π_k. The quantity P_{0k} is the transition pressure for vanishing temperature T. A nondimensional transition width is denoted by d_k. The quantity γ_k represents the Clausius–Clapeyron slope for the kth phase transition. Γ_k and π_k have been introduced by *Richter* [1973] and *Christensen* [1985b]. Because of the very high Prandtl number we use the following version of momentum balance

$$0 = -\frac{\partial}{\partial x_i}(P - P_r) + (\rho - \rho_r)g_i(r) + \frac{\partial}{\partial x_k}\tau_{ik} \tag{5}$$

accepted for publication in JOURNAL OF GEOPHYSICAL RESEARCH , 6 May 2008

The conservation of angular momentum is guaranteed by the symmetry of the stress tensor. Furthermore, the conservation of four sums of the number of atoms of the pairs $^{238}U-^{206}Pb$, $^{235}U-^{207}Pb$, $^{232}Th-^{208}Pb$, and $^{40}K-^{40}Ar$ is ensured by the numerical treatment of the chemical differentiation in Appendix A.

2.2. Viscosity, Yield Stress, and Phase Transitions

[16] The viscosity law of this paper is presented as follows. Based on experimental results of *Karato and Li* [1992], *Karato and Wu* [1993], and *Li et al.* [1996], we assume Newtonian solid-state creep for the Earth's mantle. The shear viscosity, η, is calculated by

$$\eta(r,\theta,\phi,t) = 10^{r_n} \cdot \frac{\exp\left(c\overline{T_m/T_{av}}\right)}{\exp\left(c\overline{T_m/T_{st}}\right)} \cdot \eta_3(r) \cdot \cdot \exp\left[c_t \cdot T_m\left(\frac{1}{T}-\frac{1}{T_{av}}\right)\right] \quad (6)$$

where r is the radius, θ the colatitude, ϕ the longitude, t the time, r_n the viscosity level parameter, T_m the melting temperature, T_{av} the laterally averaged temperature, T_{st} the initial temperature profile, T the temperature as a function of r, θ, ϕ, t. The quantity r_n of the first factor of the right-hand side of equation (6) has been used for a stepwise shift of the viscosity profile to vary the averaged Rayleigh number from run to run. The second factor attempts to capture the increase in the viscosity profile resulting from the cooling of the Earth. According to *Yamazaki and Karato* [2001], an appropriate value for $MgSiO_3$ perovskite is $c = 14$, and for MgO wüstite is $c = 10$. So the lower mantle c should be somewhere between these two values. For numerical reasons, we are restricted to a value of $c = 7$.

[17] The quantity $\eta_3(r)$ is the viscosity profile at the initial temperature and for $r_n = 0$. That is, $\eta_3(r)$ describes the dependence of viscosity on pressure and mineral phase. The derivation of $\eta_3(r)$ is provided in *Walzer et al.* [2004a]. In that paper, we start from a self-consistent theory using the Helmholtz free energy, the Birch–Murnaghan equation of state, the free-volume Grüneisen parameter and *Gilvarry*'s [1956] formulation of Lindemann's law. The viscosity is calculated as a function of melting temperature provided by Lindemann's law. We use pressure, P, bulk modulus, K, and $\partial K/\partial P$ from the seismic model PREM [*Dziewonski and Anderson*, 1981] to obtain the relative variation in radial viscosity. To set the absolute scale of the viscosity profile, we choose $\eta_3 = 3.45 \times 10^{20}$ Pa s at 367 km depth. This assumption yields an asthenospheric average viscosity of 10^{21} Pa s corresponding to the widely accepted value from postglacial uplift. Because we allow variation of r_n, the exact choice is not so crucial.

[18] For the uppermost 285 km of the mantle (including crust), an effective viscosity, η_{eff}, was implemented where

$$\eta_{eff} = \min\left[\eta(P,T), \frac{\sigma_y}{2\dot{\varepsilon}}\right] \quad (7)$$

where P is pressure and $\dot{\varepsilon}$ is the second invariant of the strain rate tensor. The quantity σ_y is a viscoplastic yield stress. This introduction of yield stress for the portion of the domain that includes the cold boundary layer allows our model to display plate-like behavior at the surface. Plate-like behavior would not occur without such a rheological treatment and without an asthenosphere.

[19] The surface temperature of the model is fixed to 288 K. We remark that the thickness and strength of the lithosphere is determined almost entirely by the viscosity profile. Implicitly, we are assuming that the water dependence of viscosity, the dehydration and chemical layering of the lithosphere are more important for the lithospheric viscosity than the temperature dependence. Beneath the lithosphere, there is a low viscosity asthenosphere down to the 410-km discontinuity. Issues relating to lithospheric and asthenospheric viscosity are discussed more thoroughly in section 3.3 in connection with the results shown in Figure 9.

[20] The seismic velocities, v_p and v_s, and the density, ρ, change abruptly at the 410-km mineral phase boundary. On the other hand, it is unlikely that activation volume and activation energy will not display jumps at phase boundaries. Therefore we should anticipate viscosity discontinuities at these boundaries that influence convection. According to our derivation [*Walzer et al.*, 2004a], the transition zone is highly viscous, at least between 520 and 660 km depth. The likelihood of a high-viscosity transition layer, that is embedded between two low-viscosity layers, is consistent with the proposition that the transition zone is composed mostly of garnet and spinel [*Meade and Jeanloz*, 1990; *Karato et al.*, 1995; *Karato*, 1997; *Allègre*, 2002]. If there are no further phase transitions in the lower mantle, except at about 2650 km depth near the D'' layer [*Matyska and Yuen*, 2005, 2006], then the viscosity must rise considerably as a function of depth because of the pressure dependence of the activation enthalpy of the prevailing creep mechanism for regions in which the temperature gradient is near to adiabatic. This implies a thick high-viscosity central region in the lower mantle. We infer a strong temperature gradient of the D'' layer which causes a rapid decrease in viscosity just above the CMB.

[21] Our $\eta_3(r)$ profile is supported by several recent studies. Inversion investigations for mantle viscosity profiles display an acceptable resolution down to 1200 km depth. For greater depths, models based on solid-state physics seem to be more reliable. *Kido and Cadek* [1997] and *Kido et al.* [1998] found two low-viscosity layers below all three oceans. The first layer is between the lithosphere and 410 km depth. The second one is between 660 and about 1000 km depth. The results of *Forte and Mitrovica* [2001] show even more similarity with our profile η_3. Their viscous flow models, based on two three-dimensional seismic models for mantle structure, reveal viscosity maxima at about 800 and about 2000 km depth. This is similar to our model for η_3 that has also two maxima in the interior, although is was derived by a completely different method. *Cserepes et al.* [2000] investigated the effects of similar viscosity profiles on three-dimensional Cartesian mantle convection in a box. In our dynamical model, we take into account the full effect of phase boundary distortion of the olivine–wadsleyite and of the ringwoodite–perovskite phase boundaries. The input parameters that define these phase transitions are provided in Table 1.

2.3. Numerical Method and Implementation

[22] Our code is a further development of Terra of *Baumgardner* [1983]. The Navier–Stokes equations as well

accepted for publication in JOURNAL OF GEOPHYSICAL RESEARCH , 6 May 2008

Table 1. Model Parameters

Parameter	Description	Value
r_{min}	Inner radius of spherical shell	3.480×10^6 m
r_{max}	Outer radius of spherical shell	6.371×10^6 m
	Temperature at the outer shell boundary	288 K
h_1	Depth of the exothermic phase boundary	4.10×10^5 m
h_2	Depth of the endothermic phase boundary	6.60×10^5 m
γ_1	Clapeyron slope for the olivine–wadsleyite transition	$+1.6 \times 10^6$ Pa K^{-1}
γ_2	Clapeyron slope for the ringwoodite–perovskite transition	-2.5×10^6 Pa K^{-1}
f_{a1}	Non-dimensional density jump for the olivine–wadsleyite transition	0.0547
f_{a2}	Non-dimensional density jump for the ringwoodite–perovskite transition	0.0848
d_1	Non-dimensional transition width for the olivine–wadsleyite transition	0.05
d_2	Non-dimensional transition width for the ringwoodite–perovskite transition	0.05
	Beginning time for the thermal evolution of the solid Earth's silicate mantle	4.490×10^9 a
	Beginning time for the radioactive decay	4.565×10^9 a
c_t	Factor of the lateral viscosity variation	1
k	Thermal conductivity	12 W m^{-1} K^{-1}
$nr + 1$	Number of radial levels	33
	Number of grid points	1.351746×10^6

as pressure and creep velocity are discretized using finite elements. We apply piecewise linear basis functions for the creep velocity and either piecewise constant or piecewise linear basis functions for the pressure. We solve the equations for pressure and velocity simultaneously by a Schur-complement conjugate-gradient iteration [*Ramage and Wathen*, 1994]. This is a further development of an Uzawa algorithm. We solve the energy equation using an iterative multidimensional positive-definite advection-transport algorithm with explicit time steps [*Bunge and Baumgardner*, 1995]. Within the Ramage–Wathen procedure, the resulting equation systems are solved by a multigrid procedure that utilizes radial line Jacobi smoothing. In the multigrid procedure, prolongation and restriction are handled in a matrix-dependent manner. In this way, it is possible to handle the strong variations and jumps of the coefficients associated with the strong viscosity gradients [*Yang*, 1997]. For the formulation of chemical differentiation, we modified a tracer module developed by Dave Stegman. This module contains a second-order Runge–Kutta procedure to move the tracer particles in the velocity field. Each tracer carries the abundances of the radionuclides. In this sense, tracers are active attributes which determine the heat production rate per unit volume that varies with time and position. The Fortran code is parallelized by domain decomposition and explicit message passing (MPI) [*Bunge*, 1996]. For the most runs, we used a mesh of 1351746 nodes. For some runs, we used a mesh of 10649730 nodes in order to check the convergence of the lower resolution runs. We found hardly any discernable differences (<0.5%) for the Rayleigh number, the Nusselt number, the Urey number and the laterally averaged surface heat flow as a function of time. The calculations were performed on 32 processors of the Cray Strider Opteron cluster at HLRS Stuttgart as well as on 128 processors of the SGI Altix 4700 at LRZ München. The code was benchmarked for constant viscosity convection by *Bunge et al.* [1997] with data of *Glatzmaier* [1988] for Nusselt numbers, peak velocities, and peak temperatures. The result is a good agreement with deviations $\leq$1.5%.

2.4. Heating, Initial and Boundary Conditions, and Chemical Differentiation

[23] We assume the Earth's mantle is heated mostly from within. This internal heating is expressed by the heat production density Q in equation (2) that is measured in W m^{-3}.

$$Q = H \cdot \rho \tag{8}$$

where H is the specific heat production with

$$H = \sum_{v=1}^{4} a_{jv} a_{ifv} H_{0v} \exp(-t/\tau_v) \tag{9}$$

[24] Table 2 presents the parameter data we use for the four major heat-producing isotopes. Here v stands for the radionuclide in the formulae, τ_v represents the decay time or the 1/e lifetime, H_o^v denotes the specific heat production of the vth radionuclide 4.565×10^9 years ago, and a_{jf}^v is the isotope abundance factor.

[25] We represent the distribution of radionuclides in the mantle by tracers. Each tracer is associated with a specific geochemical principal reservoir. Because of mixing, the boundaries of these reservoirs become blurred with time. In principle, even a total mixing and homogenization of the mantle is possible if the dynamic system of the mantle allows this process. Each tracer is identified by a tracer index. The reservoir concentrations of elements are given by Table 3. The lower five elements of Table 3 serve only for the computation of concentration maps but not for the calculation of heating energy either because the contributions of these elements are too low or because they are daughter nuclides. Since the relative masses of HIMU, EM1 and EM2 are small they have been neglected in the calculated model of this paper. Our model mantle starts with a uniform distribution of exclusively type-1 tracers, i.e., we start with a pure BSE mantle. If the modeled temperature, T, approaches the melting temperature, T_m, in

Table 2. Data of the Major Heat-Producing Isotopes

Isotope	^{40}K	^{232}Th	^{235}U	^{238}U
v	1	2	3	4
τ_v, Ma	2015.3	20212.2	1015.4	6446.2
H_{0v}, mW/kg	0.272	0.0330	47.89	0.1905
a_{ifv}	0.000119	1	0.0071	0.9928

accepted for publication in JOURNAL OF GEOPHYSICAL RESEARCH , 6 May 2008

Table 3. The Abundances $a_{\mu\nu}$ of the Major Heat-Producing Elements (in ppm)

Reservoir	Primordial Mantle	Oceanic Crust [MORB]	Continental Crust	Depleted MORB Mantle
Tracer index	(1)	(2)	(3)	(4)
Element				
U	0.0203	0.047	0.94	0.0066
Th	0.0853	0.12	4.7	0.017
K	250.0	600.0	9460.0	110.0
Pb	0.1382	0.30	7.0	0.035
Sm	0.4404	2.63	4.62	0.378
Nd	1.354	7.3	25.5	0.992
Rb	0.635	0.56	35.5	0.112
Sr	21.0	90.	310.	16.6

a certain volume then chemical differentiation takes place. Plateau basalts quickly rise to form the plateaus as a terrane or preliminary form of continental crust (CC) leaving behind depleted MORB mantle (DMM). The numerical conditions for this simplified chemical differentiation process will be given below. We do not use a detailed melt extraction equation system like the two-dimensional code of *Schmeling* [2006] since, for a three-dimensional spherical shell code, this would require more computational resources than we currently have available.

[26] We chose *McCulloch and Bennett* [1994] reservoir abundances for our models because of the good internal compatibility of this geochemical model. These abundances are similar to those proposed by other investigators. *Heier* [1978], *Taylor and McLennan* [1985], *Hofmann* [1988], *McCulloch and Bennett* [1994], *Wedepohl* [1995], and *Rudnick and Fountain* [1995] have suggested values for the continental crust K:U ratio of 10777, 10020, 10000, 10064, 10020, 11092, respectively.

[27] The spherical shell of our present model has free-slip and impermeable boundary conditions for both the Earth's surface and CMB. The upper surface is isothermal at 288 K. The CMB is also isothermal spatially, but not with respect to time. Applying a cooling core–mantle evolution model [*Steinbach et al.*, 1993], we adjust the CMB temperature, T_c, after each time step according to the heat flow through the CMB. We assume a homogeneous core in thermodynamic equilibrium similar to the approaches of *Steinbach and Yuen* [1994] and *Honda and Iwase* [1996]. Prior to this work, our modeling efforts relating to the problem of integrated convection–fractionation were restricted to two dimensions [*Walzer and Hendel*, 1999; *Walzer et al.*, 2004b].

3. Results

3.1. Plate-Like Motions at the Surface

[28] There are different approaches to construct mantle convection models. If we are mainly interested in understanding the physical mechanism in detail it is appropriate to devise simple models and to investigate only the influence of the variation of one parameter or to introduce only one additional effect. Even if we would individually study each of the relevant effects it would be impossible to forecast the behavior of a complex model in detail. Therefore it is geophysically legitimate to construct more complex models step by step. In this way it is possible to investigate the interplay of the different effects and to find out by variation of the parameters which effect is more relevant for the geophysical phenomena. In this more complex case it is, of course, impossible to give a verbal description of all the connections of cause and effect in detail. However, also for such models, we can outline the physical effects roughly but not in detail. Figure 1 refers to such an interim model of our present one. The interim model does not contain chemical differentiation and continents. Analogous to the three-dimensional box simulations of *Tackley* [2000a], the upper panel of our Figure 1 shows the present-day viscosity distribution at the surface of the sphere. The yield–stress mechanism (cf. equation (7)) generates the elongated, divergent and convergent zones by viscosity reduction. This means the rock cannot endure arbitrarily high shear stress and will soften at zones of maximum shear stress. Arrows denote the creep velocity. The upper panel presents the state after about 4500 Ma of thermal evolution. In the major part of the surface, the arrows indicate strong plate-like segments, separated by elongated, weak and deforming boundary zones. *Kohlstedt et al.* [1995] concluded from experiments that the rheology of the oceanic lithosphere is more complicated than that one we have been able to introduce into our model. In a more detailed model, a top layer of the oceanic lithosphere should be determined by a brittle–failure rheology, a central segment by brittle–ductile behavior and, finally, a lower layer by fully ductile behavior. Since our efforts toward a regional grid refinement are not yet finished, we could not include such kind of stockwork rheology in the present model. In Appendix B we describe in which direction we are working to refine the results in future models. Since we simply used a yield–stress criterion, the upper panel of Figure 1 does not show any strike–slip zones or transform boundaries. Furthermore, the divergent and convergent zones are too broad, yet. To form a more realistic model in the meantime until the final development of our grid refinement tools, we introduced a thin rigid crust with brittle fracture lines at the surface, the positions of which are determined as a freely developing function of time without giving up the internal dynamics and the yield–stress mechanism of the preceding step of the model. At first we present some preliminary considerations. The following applies for an idealized plate tectonics with sharp boundaries. If we plot the divergence

$$\mathrm{divh}\,\vec{v} = \nabla_h \cdot \vec{v} = \frac{1}{r_0}\left[\cot\theta \cdot v_\theta + \frac{\partial v_\theta}{\partial \theta} + \frac{1}{\sin\theta}\cdot\frac{\partial v_\phi}{\partial \phi}\right] \qquad (10)$$

as a pseudotopography on the spherical surface then the divergent and convergent plate boundaries will appear as linear mountain crests or hogbacks. For conservative plate boundaries, the curl

$$\mathrm{roth}\,\vec{v} = (\nabla \times \vec{v})_h = \frac{1}{r_0}\left[\cot\theta \cdot v_\phi + \frac{\partial v_\phi}{\partial \theta} + \frac{1}{\sin\theta}\cdot\frac{\partial v_\theta}{\partial \phi}\right] \qquad (11)$$

will produce mountain crests in the respective pseudotopography. The velocity components v_r, v_θ and v_ϕ are assigned to radius r, colatitude θ and longitude ϕ. The Earth's radius

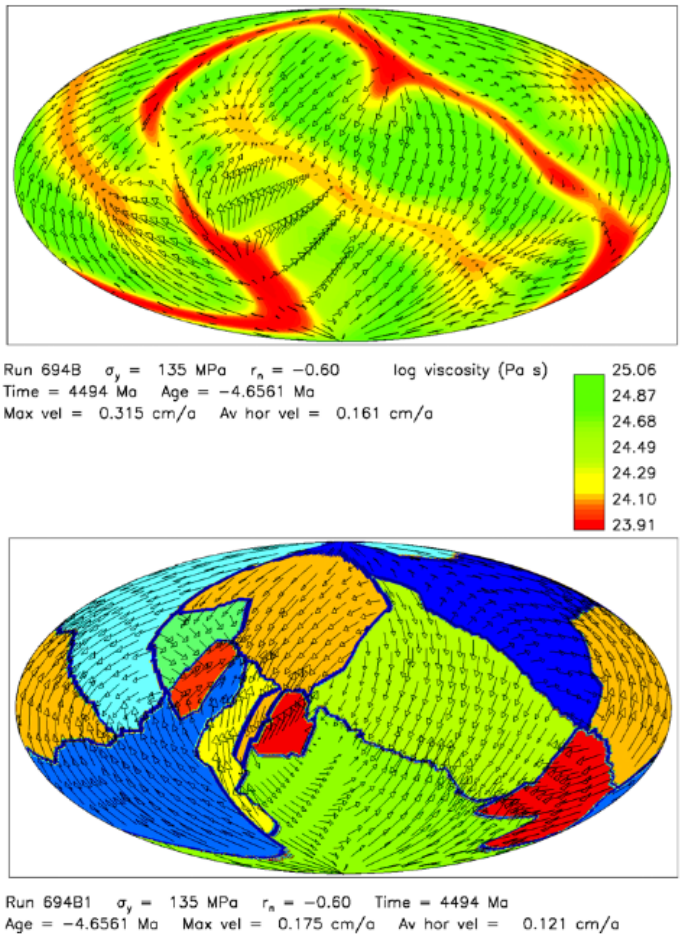

Figure 1. The first panel shows an equal-area projection of the present-day surface viscosity distribution (colors) and the creep velocities (arrows) for a preliminary model without chemical differentiation and without continents, case 694B with $\sigma_y = 135$ MPa, and $r_n = -0.60$. For comparison, the second panel presents the refined plates for case 694B1, also without differentiation and continents.

is denoted by r_0. At all plate boundaries, the surface expression of the square root of the second invariant of the strain rate tensor, *invh* $\vec{v}$, must generate mountain crests where

$$\text{invh}\,\vec{v} = \dot{\epsilon}_{surf} = \frac{1}{r_0}\left[\left(\frac{\partial v_\theta}{\partial \theta}\right)^2 + \left(\frac{1}{\sin\theta}\cdot\frac{\partial v_\phi}{\partial \phi} + v_\theta\cdot\cot\theta\right)^2 + \frac{1}{2}\left(\frac{1}{\sin\theta}\cdot\frac{\partial v_\theta}{\partial \phi} + \frac{\partial v_\phi}{\partial \theta} - v_\phi\cdot\cot\theta\right)^2\right]^{1/2} \quad (12)$$

We calculate the crest lines of the invh-mountains and define idealized plate boundaries by these lines which are movable. Each movement along the spherical surface can be represented by an angular velocity of a rotation around the Earth's center. We average these angular velocities, $\vec{\omega}$, of all the surface grid points which belong to one idealized plate. So a unified angular velocity, $\vec{\omega}_u$, is assigned to each plate. The movability of the plate boundaries is not restricted by this procedure. The lower panel of Figure 1 reveals the new plate distribution for comparison with the upper panel. Neighboring plates have different angular velocities, $\vec{\omega}_u$. Sometimes we can observe nearly strike–slip zones, e.g., in the second panel of Figure 1, in the left lower quadrant between the small yellow plate and the large green plate on the right hand side. Figure 2 shows that the plate-building mechanism is not affected by the further development to a

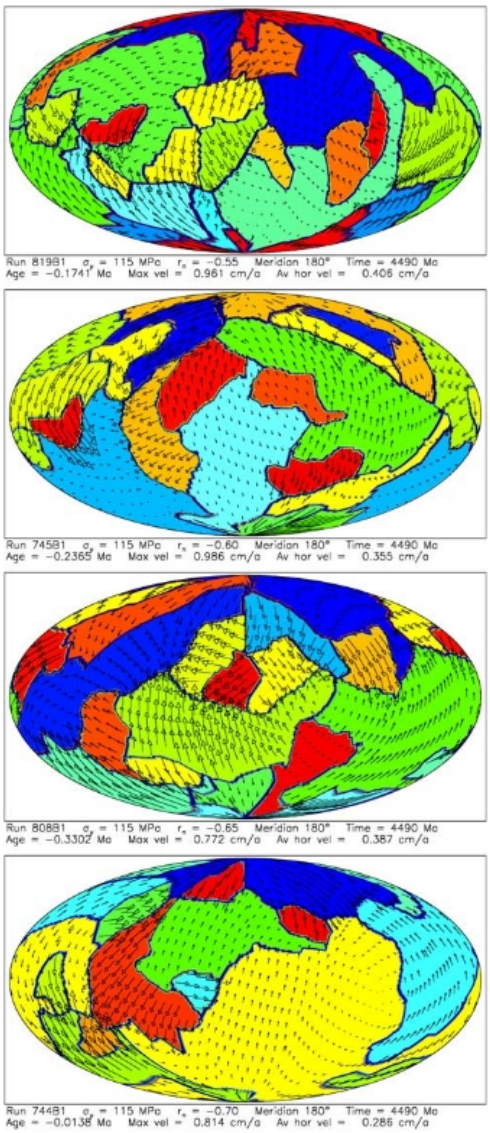

Figure 2. Lithospheric plates (colors) and creep velocities (arrows) for the present model with chemical differentiation and continents, which are not shown here but in Figure 6. The parameter r_n is varied in equal steps. For decreasing r_n, the viscosity difference between lithosphere and asthenosphere proves to be increasing and the number of plates decreases if apart from that all other parameters are fixed.

convection model with continents which are generated by chemical differentiation and the accretion of oceanic plateaus. In Figure 2, the yield stress is fixed at σ_y = 115 MPa and the viscosity-level parameter, r_n, is varied with equal intervals. According to equation (6), the mean viscosity of case 744B1 (lowermost panel) is only 70% of the mean viscosity of case 819B1 (uppermost panel). We compare the distributions of lithospheric plates after 4490 Ma of evolution. At several locations, there are nearly strike-slip zones, e.g., in case 808B1 (third panel of Figure 2) near the north pole between the light-blue plate on the right hemisphere and the steel-blue plate on the left hemisphere. Plate and bulk convection are no separate entities in our model but form an integrated convective system. Section 3.3 shows that the generation of oceanic lithosphere is essentially influenced by devolatilization and chemical layering whereas the asthenosphere is mainly produced by the distribution of water abundance in relation to the radial dependence of water solubility. So neither oceanic lithosphere nor asthenosphere are generated only by the temperature dependence of viscosity. Our model roughly reflects these findings. We found by many numerical experiments that our kind of plate generation works without and with continent generation by differentiation. For purely viscous rheology without asthenosphere, we could not produce any plates. However, this latter finding confirms only the results of other authors (cf. section 1.3). Section 3.4 shows by variation of parameters which regions of temporally averaged Rayleigh number and viscoplastic yield stress are able to generate plate tectonics. In equatorial and meridional sections, we found cold sheet-like currents in the upper mantle and in the upper parts of the lower mantle. However, the model does not furnish us with subduction zones sloping against the continents. So the problem of subduction asymmetry is not solved. In our model, all plate-like σ_y–Ra solutions begin to show plate-like behavior already in the Archean. Movements, size and form of the plates prove to be variable as a function of time but the plate tectonics is continuous. So for a run which is plate-like in the present time, we do not find any other convection regime for earlier times. As already mentioned in the deduction of our viscosity profile [*Walzer et al.*, 2004a], a strict self-consistent solution of the plate-initiation problem will only be possible if the endogenic cycle of volatiles, especially of water, is included. It is surely not coincidental that the only terrestrial planet with a present-day ocean shows plate tectonics. The initiation might demand hydrolytic softening [*Regenauer-Lieb et al.*, 2001]. Since the growth of the continental crust is the focus of our paper, we will not deal more extensively with the plate generation problem.

3.2. Further Results: Predictable and Stochastic Features of the Model

[29] Our convection–differentiation mechanism is partly predictable and partly stochastic. Essential features are predictable although the model as well as the real Earth show stochastic features at bifurcation points. The connection between bifurcations and stochasticity scenarios is the principal reason why the treated system cannot be entirely predictable [*Monin*, 1990; *Gallavotti*, 2002]. The variable Rayleigh number, Ra_i, is a function of time, essentially

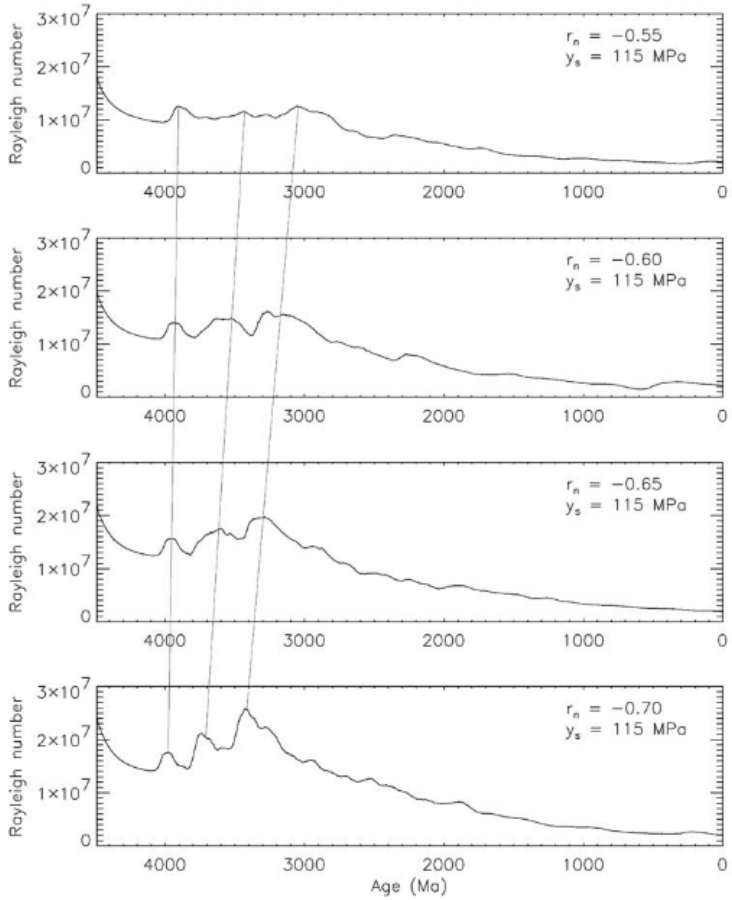

Figure 3. A variation of the viscosity level parameter, r_n. The time evolution of the variable Rayleigh number, Ra_t, of the cases show predictable shifts of prominent features as a function of r_n.

because of the temperature dependence of viscosity. The spatially averaged mantle viscosity increases since the Earth is cooling. This is essentially expressed by the second factor of the right hand side of equation (6). Therefore Ra_t decreases in the main part of the evolution time. However, in some time intervals we observe a Ra_t growth due to feedback effects. These relatively short time intervals can be explained by regroupments of the plates at the surface and connected feedback effects. Is it possible to predict the position of these individual rises on the time axis using the form of the Ra_t curves of neighboring runs? Figure 3 presents a series of $Ra_t(t)$ evolutions for an equidistant succession of r_n values. The yield stress, σ_y, is kept constant. It is shown that the shift of the Ra_t maxima is a nearly linear function of the viscosity level parameter, r_n. It is remarkable that these maxima are predictable for new neighboring runs between the presented ones. The temporally and spatially averaged viscosity of the bottom panel of Figure 3 is by a factor of about 0.7 lower than the temporally and spatially averaged viscosity of the uppermost panel. Therefore the sequence of high-Ra_t events is accelerated from the top to the bottom panel. Figure 3 shows the Ra_t evolution for four combinations of the parameters (r_n, σ_y) with equal r_n distances. The final distribution of plates and surface creep velocities after 4490 Ma of solid mantle evolution is demonstrated for the same four combinations by Figure 2. Furthermore, we observe that the difference between maximum lithospheric viscosity and minimum asthenospheric viscosity grows with decreasing r_n. This is connected with the observation that the number of plates is decreasing from top to bottom panel of Figure 2. However, this is only a rule because of

fluctuations. For a strong growth of the lithospheric viscosity we should evidently expect a limit where a one-plate planet is achieved.

[30] As a resolution test and in search of stochastic features, we performed each run twice with a differing number of tracers. We used about 10.5 million tracers for basic runs (B-runs) and about 84 million tracers for comparative runs (C-runs). In Figure 4, we show three columns of time evolutions of the variable Rayleigh number, Ra_r, for the parameter r_n fixed in each column. The parameter r_n mainly determines the level of the temporally and spatially averaged viscosity. The deviations between B-runs and C-runs seem to be mainly stochastic. The temporal positions of the first three main maxima of $Ra_t(t)$ in the first column have a scarcely perceptible dependence on the viscoplastic yield stress. The corresponding features occur somewhat later for higher yield-stress values since it takes more time to achieve the threshold shear stress which is necessary to generate a zone of viscoplastic flowability. The other two columns of Figure 4 show this weak dependence, too. However, a comparison of the prominent features of the curves between the first, second, and third columns and other columns not shown here corroborates the strong dependence of the temporal shift of the maxima of $Ra_t(t)$ as a function of the viscosity-level parameter, r_n.

[31] Figure 5 reveals the production of juvenile continental mass by chemical differentiation of the mantle. The total growth rate within each 25-Ma interval is converted to 10^{18} kg/Ma and graphically represented by a point. The points have been linearly connected. At least in the first two peak groups of the evolution, the conversion curves are similar. For this reason and because of the large number of tracers, it is evident that the curves are not merely an expression of numerical discretization noise despite the episodic character of the curves. It is obvious that stochastic processes occur both in the real mantle and in the model at bifurcation points etc. In the first column of Figure 5, the viscosity-level parameter is fixed at $r_n = -0.60$. The yield stress decreases in equidistant steps from $\sigma_y = 135$ MPa for the top panel to $\sigma_y = 115$ MPa for the bottom panel. The first group of peaks shows a very weak dependence on yield stress. The second peak group occurs about 40 Ma earlier in the bottom panel compared to the corresponding feature of the top panel. This is in accord with the results of Figure 4. For the third group of maxima, we observe a slight shift in a similar order of magnitude. The distribution of later growth episodes is more or less noncorrelated. Compared to the $Ra_t(t)$ curves, the course of chemical differentiation shows considerably higher portions of stochastic behavior. Similar conclusions can be found for the second and third columns of Figure 5. In the third column, the second group of peaks of the bottom panel, for $\sigma_y = 115$ MPa, occurs about 70 Ma earlier than the second group of the top panel, for $\sigma_y = 135$ MPa. The first group of maxima of the chemical differentiation in the third column of Figure 5 begins earlier than that of the first column since the spatial average of viscosity is lower, independent of the variation of yield stress. This observation corresponds to the behavior of $Ra_t(t)$ curves. So the evolution of differentiation of the third column of Figure 5 is more rapid than that of the second column and even quicker than that of the third column. This corresponds to the $Ra_t(t)$ behavior of Figure 4. The lower the mean viscosity is, the earlier is the onset of differentiation peaks of Figure 5 assigned to each other.

[32] To sum up it can be said that the evolution of the Rayleigh number is more predictable than that of the episodes of the generation of juvenile continental material. The evolution of chemical differentiation of oceanic plateaus, however, has also deterministic portions but it is considerably more stochastic than $Ra_t(t)$. If we suppose an equal initial state in the whole spherical shell for each run, then the time position of elevated activity of chemical differentiation is predictable only for the first two groups. However, this strong limitation of predictability does not apply for the integrated mass of differentiated material. The latter statement is in agreement with the observation of rather good predictability of the temporal course of Ra_r. Cf. Figure 3. So the low predictability of the time distribution of juvenile growth batches does not mean that the total mass of the continents is not rather predictable for fixed time t, r_n, and σ_y. Cf. Figure 13. Also, the number of continents and their connectivity is to a certain degree predictable (cf. Figure 12). Only the exact distribution of continents and their spherical harmonics coefficients have a rather stochastic distribution for the present time but we can find solutions similar to the observed ones. The exact continent distribution of the real Earth might be also not predictable in this sense even with known initial conditions of the mantle's evolution.

3.3. Episodic Growth of the Continental Crust

[33] Notably, the curves of Figure 5 qualitatively resemble those of observed episodic continental growth [*Condie*, 1998; *Kemp et al.*, 2006]. *Parman* [2007] showed that not only the production peaks of OIB but also those of MORB can be correlated to the zircon-age peaks. This observation argues for episodic mantle melting and crustal growth. This suggests that, similar to our model, the continental crust was not generated entirely at the beginning but instead evolved episodically in batches, distributed in time over Earth's history. The variation of the yield stress, σ_y, and the viscosity-level parameter, r_n, leads to continent-growth curves becoming more and more stochastic for later times. Therefore one cannot forecast the temporal position of main peaks of the converted continent-tracer mass growth for times near the present time using runs in the $r_n - \sigma_y$ neighborhood. From fundamental fluid-dynamical investigations [*Gallavotti*, 2002] it follows that this kind of stochasticity might also apply for these growth curves of the real Earth. For this theoretical reason it should not be expected that neighboring curves of Figure 5 have nearly coinciding main peaks and that the detailed present-day continent distribution belonging to it is also not predictable.

[34] Figure 6 reveals the present-day distribution of continents (red). The oceanic plateaus (black dots) are carried along by a nearly self-consistently generated, moving oceanic lithosphere (yellow). Whenever the plateaus touch a continent they have to join with it. This is the only additional implementation. Depleted parts of the mantle with more than 50% depleted MORB mantle are depicted in yellow. DMM dominates below the lithosphere near the surface because DMM is generated near the surface. The depleted, "yellow" material is subducted jointly with the

accepted for publication in JOURNAL OF GEOPHYSICAL RESEARCH , 6 May 2008

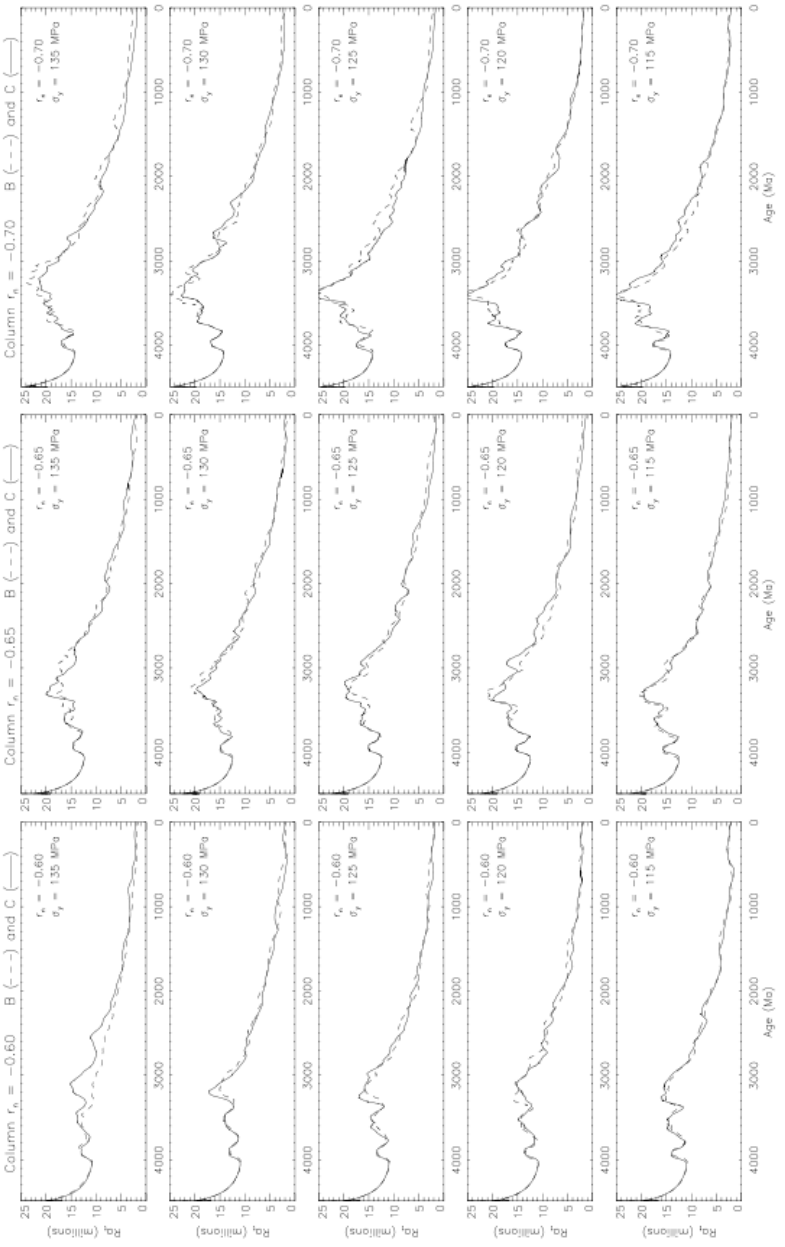

Figure 4. The Rayleigh number, Ra_i, as a function of time. In the first column, the viscosity level parameter, r_n, is kept constant at −0.60, in the second column at −0.65, and in the third column at −0.70. Within each column, the yield stress varies from 135 MPa in the uppermost panel to 115 MPa (bottom). Dashed lines signify B-runs; solid lines represent C-runs.

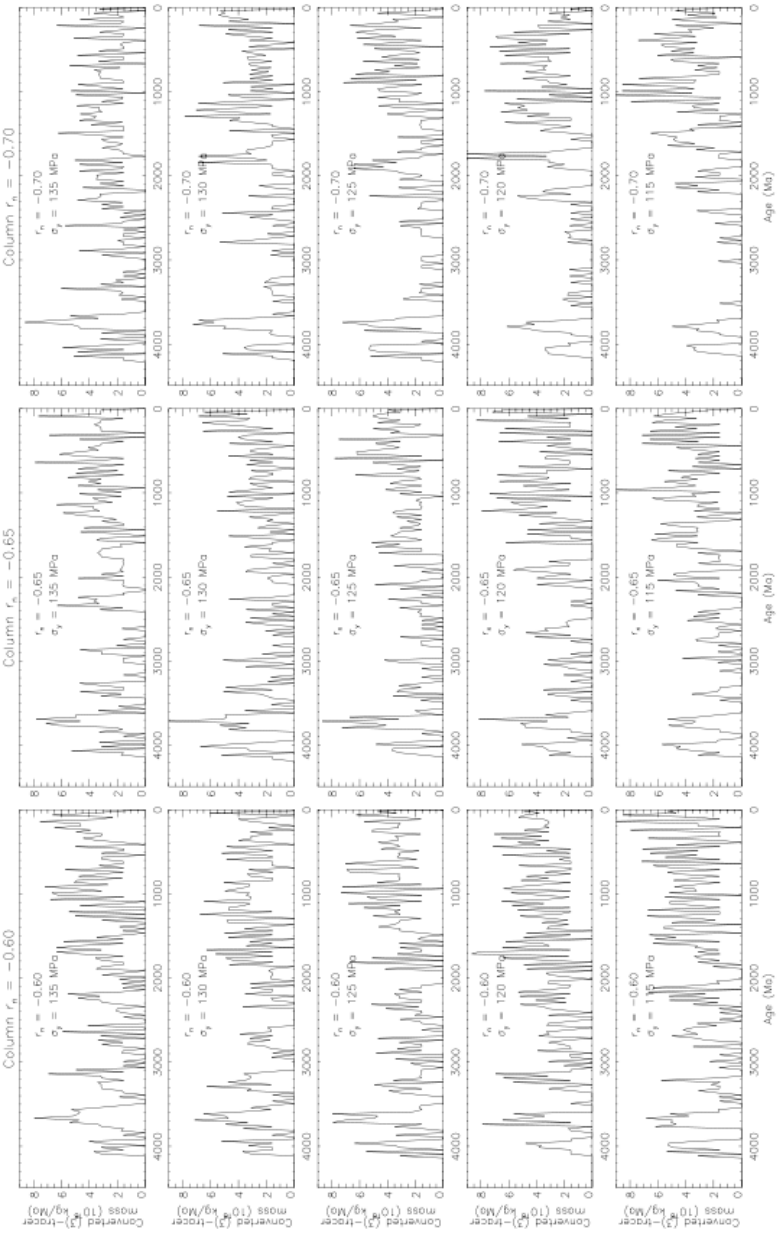

Figure 5. Time evolution of the juvenile contributions to the total mass of the continents. Comparison of various runs with different yield stress, σ_y, and different viscosity-level parameter, r_n. The lower r_n is the higher is the temporally averaged Rayleigh number. The rate of the converted continental-tracer mass has been averaged for every 25 Ma and plotted in discretized form. We converted the total mass growth of the continents into units of 10^{18} kg/Ma.

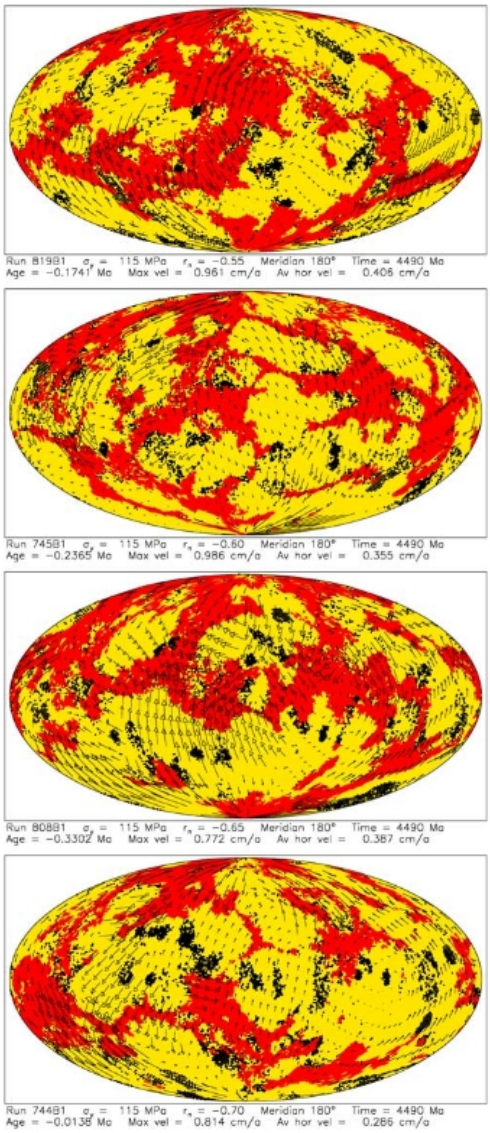

Figure 6. Continents (red), oceanic lithosphere (yellow), and oceanic plateaus (black dots) for the present time. Arrows are a measure of surface creep velocities. These runs have the same yield stress, σ_y = 115 MPa. First, second, third, and fourth panel differ among one another only by the viscosity-level parameter −0.55, −0.60, −0.65 and −0.70, respectively (cf. Figures 2, 3, and 7).

high-viscosity surface plates into the mantle. When cut crosswise by the equatorial section, partially disintegrated slabs are visible as a yellow stripes. It is remarkable that, in spite of 4500 Ma of solid-state mantle convection, chemical reservoirs continue to persist. DMM predominates not only beneath the oceanic lithosphere, but also immediately below the continents (red). This is a realistic feature of the model since it is observed that where the real oceanic lithosphere is rifted, MORB magma is formed by decompression melting. The MORB source (DMM) is not only depleted in incompatible elements but also relatively homogenized. It is homogenized not only with respect to its major geochemical components (SiO_2, MgO, FeO, Al_2O_3, CaO [*Palme and O'Neill*, 2003]) but also with respect to isotope ratios $^{87}Sr/^{86}Sr$, $^{143}Nd/^{144}Nd$, $^{206}Pb/^{204}Pb$, $^{207}Pb/^{204}Pb$ and $^{208}Pb/^{204}Pb$. As a consequence, the standard deviation of these isotope ratios and of the major element compositions is small for MORBs in comparison to OIBs [*Allègre and Levin*, 1995] although *Hofmann* [2003] has modified this conclusion somewhat.

[35] The present-day proportion of DMM in the real Earth's mantle is not exactly known. Estimates depend on which element is used and its assumed abundance in CC and DMM. If samarium and neodymium are not so extremely enriched in CC, then smaller volumes of DMM are possible. Calculations using Cs, Rb, Th and K suggest 50% of the mantle is DMM. *Bennett* [2003] estimated that between 30% and 60% of the mantle is depleted if an intermediate degree of depletion of DMM is assumed. *Hofmann* [2003] deduced a depleted reservoir of the mantle between 30% and 80%.

[36] Figure 6 displays the present-day continent configurations of the same σ_y–r_n combinations which have been used in Figure 2. Arrows denote the plate velocities at the surface. At some locations, the oceanic plate subducts at the margin of a continent, e.g., in the first panel of Figure 6 (Run 819B1) near the equator at the right-hand margin of the ellipse which is generated by equal-area projection from the surface of the sphere. There is a yellow ocean bottom quickly moving to SSW and coming to an end by subduction at the right red continent. In the second panel of Figure 6 (Run 745B1) in the right upper quadrant, an oval-shaped yellow oceanic plate with NW velocity terminates at the upper continental stripe. In the fourth panel of Figure 6 (Run 744B1) an oceanic lithosphere plate with SW velocity ends at a large continent situated at the far left margin of the projection. We observe also continent–continent collisions, e.g., in the third panel of Figure 6 (Run 808B1) between the large, essentially oceanic plate on the southern hemisphere with NNW velocity and the large continent north of it. We note that convergent plate boundaries also occur in the interior of continents of the real Earth, e.g., the Transhimalayan Suture Zone or the Zagros Suture Zone. In the same panel, we observe a small ocean–ocean collision in the very right part of the right upper quadrant between a northward moving yellow oceanic plate near the equator and a SE moving small oceanic plate north of it.

[37] In the present-day real Earth, the continent–ocean collision case occurs more frequently than in the sum of our runs. This might have two reasons. Firstly, continental and oceanic lithosphere thicknesses are equal in our present model. Secondly, we use a not only temporally but also

accepted for publication in JOURNAL OF GEOPHYSICAL RESEARCH , 6 May 2008

laterally constant yield stress. We expect the subduction zone will evolve mainly at the continental margin in a future model if we suppose a lower σ_y in a narrow stripe parallel to the freely evolving margin whereas σ_y is higher in the interior of the continents and oceanic plates. Since we suppose constant thickness of the lithosphere in the present model, we could not study the global warming of the mantle beneath large continents. *Lenardic et al.* [2005] and *Coltice et al.* [2007] investigated this effect.

[38] We ran each of our cases to a time of 4.5 billion years to compare our model results with observations of the present Earth and with the Earth's evolution as far as possible. We track the time evolution of Rayleigh number, Ra_t, Urey number, *Ur*, and the laterally averaged heat flow, *qob*, in our runs and compare them with the results of other authors. Figure 3 shows the variation of Rayleigh number, Ra_t, with time for the four cases of Figure 6. The different panels represent different values for the viscosity-level parameter, r_n. To avoid numerical instability, we were restricted to Rayleigh numbers somewhat smaller than those estimated for the real Earth. In our earlier two-dimensional models, we could achieve higher Rayleigh numbers but also in this case we had to be careful to avoid spikes produced by numerical discretization noise in the various evolution curves. The physical reasons of the three main Ra_t peaks are feedback effects which are connected with reorganization of the mantle flow patterns and of the lithospheric plate movements. Figure 4 represents other σ_y–r_n combinations. The deviations of the C-curves from the B-curves in Figure 4 are almost certainly a result of stochastic effects. Of course, they are small at the beginning of the run since we used the same initial conditions for B- and C-runs. Note that the locations of the maxima of Ra_t on the time axis depend on viscosity but very little on yield stress. The quantity τ denotes the age. If we compare only runs with a fixed yield stress σ_y = 120 MPa, peaks of $Ra(\tau)$, assigned to each other, are situated approximately at τ = 2700 Ma for the panel column with $r_n = -0.45$, at τ = 2860 Ma for $r_n = -0.50$, at τ = 3010 Ma for $r_n = -0.55$, at τ = 3100 Ma for $r_n = -0.60$, at τ = 3370 Ma for $r_n = -0.65$ and finally at τ = 3410 Ma for $r_n = -0.70$. Because of space limitations, we do not show the plots of $Ra(\tau)$ for the viscosity-level parameters −0.45, −0.50 and −0.55. The described shift of the peak as a function of r_n is easy to understand since the lower the average viscosity the earlier the Ra_t curve reaches its relative peak value. The shift in the location of these peaks is rather regular so that it can be predicted for other parameter choices. The maxima become more distinct with lower r_n.

[39] In Figure 7 we present the laterally averaged heat flow, *qob*, as a function of time for various values of the viscosity-level parameter, r_n. For comparison, the runs have the same order as in Figures 2, 3, and 6. Comparison of the dashed curves for B-runs and solid lines for C-runs shows how the details of the time history are affected by the density of active tracers. All curves reach realistic values for the present time. The observed mean global heat flow has been estimated to be 87 mW/m^2 [*Pollak et al.*, 1993]. The model automatically yields such values when the usual abundances of incompatible elements are adopted, such as those of *McCulloch and Bennett* [1994] or *Hofmann* [1988], etc. In this paper, we use the values of *McCulloch and Bennett* [1994]. It is remarkable that the course of the $qob(\tau)$-curves do not vary essentially from top to bottom panel of Figure 7, i.e., in the direction of decreasing mean viscosity. Figure 2 shows, however, a decrease of the number of plates in this direction. It is evident that the heat flow heavily depends on the abundances of heat-producing elements whereas the number of plates is more influenced by the viscosity distribution near the surface.

[40] We would like to comment on the physical reason why the $qob(\tau)$ curves of Figure 7 are more realistic than the corresponding curves of the parameterized models that typically display a much steeper decrease in the surface heat flow. It is generally accepted that the continental lithosphere is a chemical boundary layer. One may conclude that the viscosity difference between continental lithosphere and the asthenosphere beneath it is mainly a consequence of the compositional contrast and only to a smaller degree a consequence of temperature difference. In this paper, we additionally assume that the viscosity contrast between oceanic lithosphere and underlying oceanic asthenosphere is determined mainly by devolatilization of H_2O, CO_2, etc., by the chemical layering of the oceanic lithosphere, and only to a certain degree by the temperature dependence [*Green and Falloon*, 1998; *Frost*, 2006]. This additional assumption is corroborated by the following results. The melting temperature, T_m, decreases by about 700 K in the presence of water [*Grove et al.*, 2006]. About 50 ppm hydrogen reduces the viscosity of olivine by a factor of 30–100 [*Mei and Kohlstedt*, 2000; *Hirth*, 2006]. If we assume that the mantle has a moderately high water content, e.g., that the present-day mantle contains more than one ocean [*Hirschmann et al.*, 2005], and that the oceanic lithosphere is dehydrated, we confidently conclude that the lithospheric and asthenospheric portion of our viscosity profile (cf. Figure 9) is realistic. Furthermore, the viscosity of lithosphere and asthenosphere depends not only directly on the absolute water content but also on the water solubility [*Mierdel*, 2006; *Keppler and Bolfan-Casanora*, 2006; *Mierdel et al.*, 2007]. It is extremely important for viscosity which of the two values is greater in which depth region. Since the water solubility has a minimum in the depth range of the asthenosphere, only a moderate water abundance is necessary to produce free water molecules at the grain boundaries. Therefore the viscosity profile will decrease dramatically in that depth interval. For that reason we expect that our derivation of the viscosity profile [*Walzer et al.*, 2004a] is justified at least in broad outline. That is, why we have partly imposed the radius-dependent factor of lithospheric viscosity (cf. equation 6). Large lateral variations of lithospheric viscosity evolve approximately along great circles which move dynamically due to the existence of the yield stress. Therefore we expect that the very large decrease of the laterally averaged heat flow as a function of time is restricted to the earliest epoch of the Earth's evolution. The surface temperature can be considered to be uniformitarian whereas the surface heat flow shows only a slow decrease with some temporal variations. In the judgment of this result, one should for fairness take into account that only the present-day value of the surface heat flow, *qob*, has been measured directly. Indirect estimates of *qob* can be inferred, e.g., for the Archean. *Takahashi* [1990] and *Nisbet et al.* [1993] estimated the Archean upper-mantle

accepted for publication in JOURNAL OF GEOPHYSICAL RESEARCH , 6 May 2008

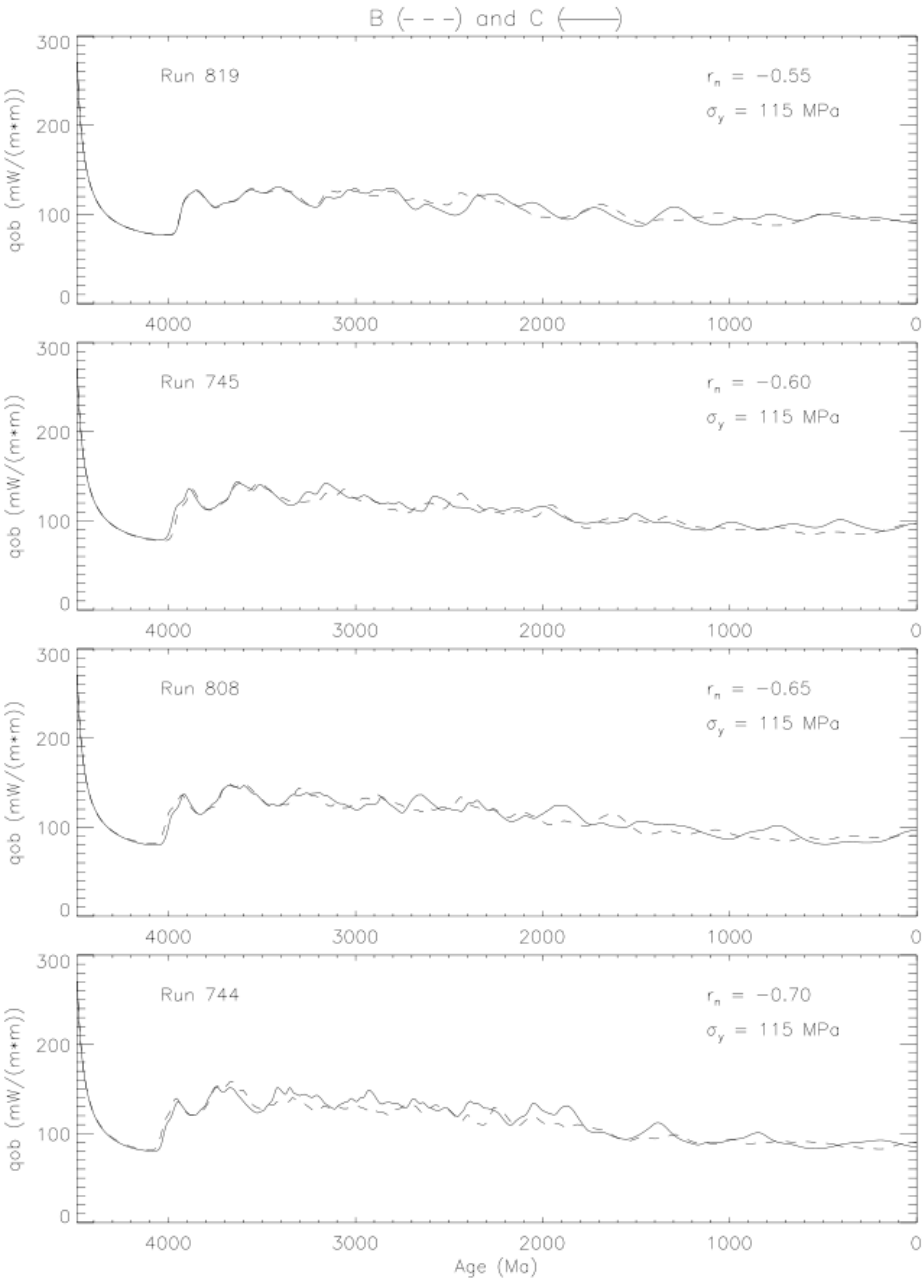

Figure 7. The evolution of the laterally averaged surface heat flow, *qob*, for neighbor runs. The parameter σ_y is kept constant at 115 MPa. The viscosity-level parameter varies from −0.55 (top) to −0.70 (bottom). Dashed lines belong to B-runs; solid lines to C-runs.

accepted for publication in JOURNAL OF GEOPHYSICAL RESEARCH , 6 May 2008

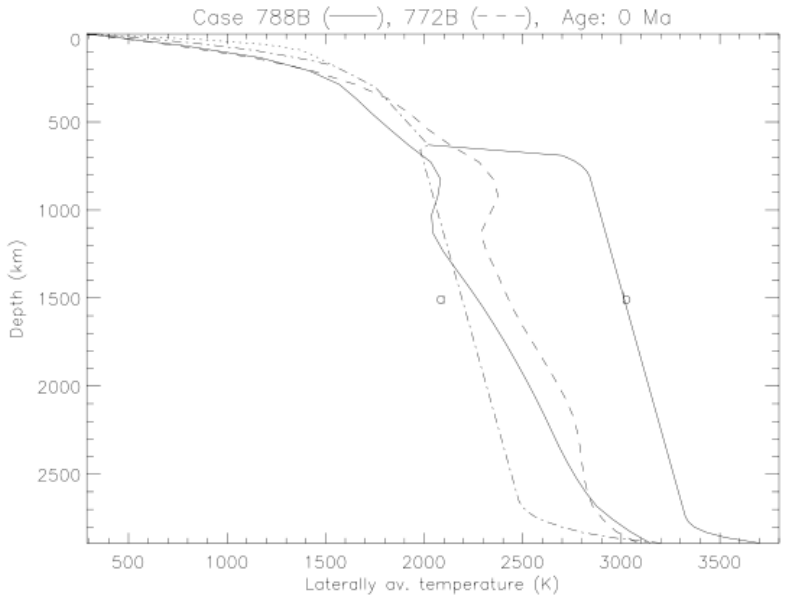

Figure 8. The laterally averaged temperature of the geological present time as a function of depth for run 788B (solid curve) with a viscoplastic yield stress, σ_y = 105 MPa, and a viscosity level parameter, r_n = −0.30, and for run 772B (dashed) with σ_y = 125 MPa and r_n = −0.60. A range of mantle geotherms using parameterized models of the mantle's thermal history given by *Schubert et al.* [2001] is depicted for comparison. Labels a and b signify geotherms of whole mantle and layered convection, respectively. The dotted line denotes a midoceanic ridge geotherm.

temperature from the composition of perioditic komatiites. They concluded that the Archean upper mantle was 600 K hotter than the present one. If one, however, supposes that komatiite was not generated from normal upper mantle but from plumes [*Parman et al.*, 1997], one arrives at lower values. Using investigations on greenstones, *Abbott et al.* [1994] concluded a temperature drop of about 250 K for the mid-Archean upper mantle to that of today. For comparison, we average the temperatures at 370 km depth for the age interval between 2500 and 4000 Ma for the presented runs and calculate the difference from the present-day temperatures of the model also at 370 km depth. The modeled temperature drop is 380–390 K. Since we obtain the heat flows shown in Figure 7 from the same model, they seem to be realistic. It is now widely accepted that komatiites are produced in a plume environment. An alternative but possibly less probable inference that komatiites are generated by hydrous melting in a subduction zone [*Grove and Parman*, 2004] results in only about 100 K temperature drop. *Komiya* [2004] arrives at 150–200 K. From all these considerations, we conclude that the parameterized models overestimate the Archean heat flow.

[41] The discussion of the influence of temperature dependence of viscosity on thermal evolution has a long history with some amount of controversy [*Tozer*, 1967; *Christensen*, 1984, 1985a; *Schubert et al.*, 2001]. This history has resulted in the discovery of three regimes, namely, the small viscosity contrast regime, the sluggish-lid regime, and the stagnant-lid regime [*Moresi and Solomatov*, 1995; *Solomatov*, 1995]. In future, the influence of volatile abundances should be systematically investigated in an analogous way.

[42] Now we want to compare two very different cases, run 788B1 with σ_y = 105 MPa and r_n = −0.30 as well as run 772B1 with σ_y = 125 MPa and r_n = −0.60. Therefore also the temperature distributions and viscosity profiles are rather different. Figure 8 shows the laterally averaged temperatures of these two cases for the present time in comparison with parameterized models [*Schubert et al.*, 2001]. Label a denotes an average parameterized whole mantle model whereas label b represents a parameterized layered convection model. As expected, our two curves lie closer to the geotherm of the parameterized whole mantle convection model than to the corresponding layered-convection temperature. This is understandable since the present model displays whole mantle flow. However, the flow is somewhat impeded by a high-viscosity transition zone and by the endothermic 660-km phase boundary. Therefore the temperature is slightly augmented, especially immediately beneath the 660-km discontinuity. Our model also includes the full effect of the phase-boundary deflection of the upper mantle. Figure 9 shows the laterally averaged viscosity for the present epoch. Derivation and discussion of the viscosity

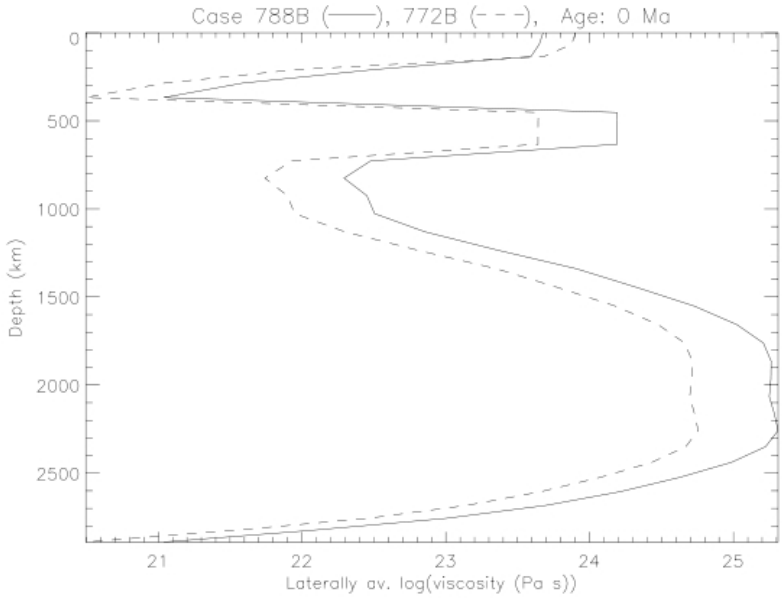

Figure 9. The laterally averaged shear viscosity of run 772B (dashed) and run 788B (solid curve) as a function of depth for the present geological time (cf. equations (6) and (7)).

profiles is given in section 2.2. Figure 10 presents the present-day distribution of continents (red), oceanic lithospheric plates (yellow) and oceanic plateaus (black). At first we judge the results of these pictures and those of other cases according to the number and connectivity of continents (cf. Figure 12) and according to the size of the sum of continents (cf. Figure 13). We do so to have a rough measure of the quality of the approximation of the observed present-day continent distribution. Cases of good quality show a cluster in these plots so that we can forecast that similar r_n–σ_y combinations will result in good solutions, too. Later we decided to represent both continental distributions in terms of spherical harmonics.

$$\{A_n^m \text{ or } B_n^m\} = \frac{\sqrt{2n+1}}{\pi\sqrt{2}} \sqrt{\frac{(n-m)!}{(n+m)!}} \cdot \int_0^{2\pi} \{\cos m\phi \text{ or } \sin m\phi\} \cdot \left[\int_0^{\pi} f(\theta,\phi) \cdot P_{n,m}(\cos\theta) \cdot \sin\theta \cdot d\theta \right] d\phi \qquad (13)$$

respectively, where $f(\theta, \phi)$ is 1 for continents and 0 for oceanic lithosphere. While the individual coefficients A_n^m or B_n^m depend on the position of the pole of the grid (θ, ϕ), the quantity h_n^* given by

$$h_n^* = \frac{\sqrt{n \cdot (n+1)}}{2} \cdot \left\{ \sum_{m=0}^{n} \left[(A_n^m)^2 + (B_n^m)^2 \right] \right\}^{1/2} \qquad (14)$$

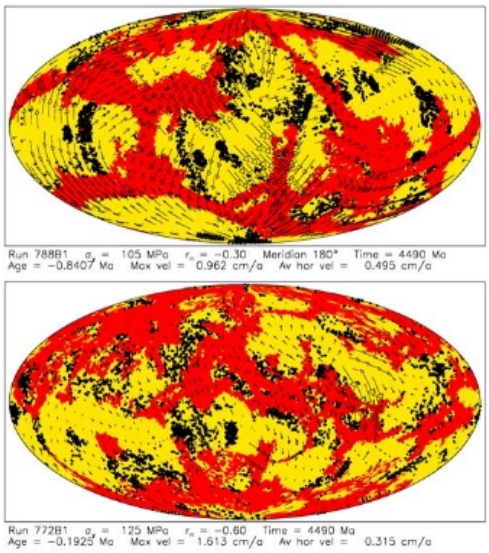

Figure 10. Present-day continents (red), oceanic lithosphere (yellow), and oceanic plateaus (black dots) for two very different runs.

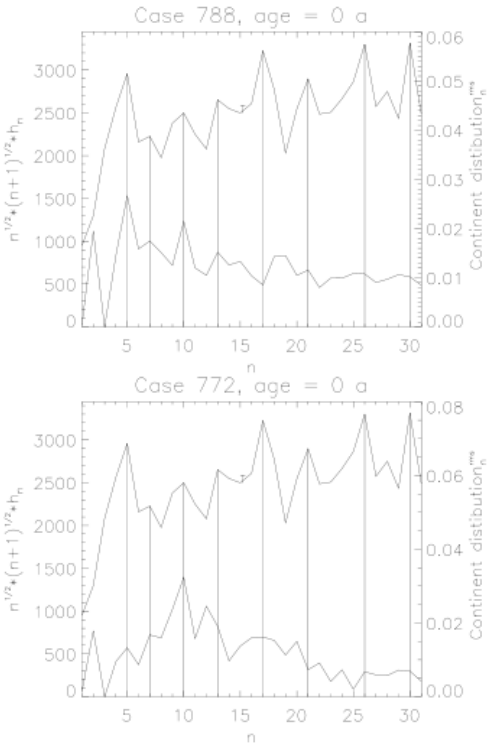

Figure 11. A comparison of the orientation-independent quantities h_n^* of the observed total topography of the Earth, *T*, with the total topography of the calculated present-day distribution of continents of the runs 788 and 772. The parameters $\sigma_y = 105$ MPa and $r_n = -0.30$ apply for case 788 (top), $\sigma_y = 125$ MPa and $r_n = -0.60$ for case 772 (bottom). We calculated the observational curve, *T*, from the topography of the global JGP95E digital elevation model by *Lemoine et al.* [1998, chapter 2].

is orientation-independent. This means that the quantity h_n^* does not depend on the position of the pole of the map grid. The spectra of the continent distribution of the cases 788B1 and 772B1 are presented by the lower curves of each panel of Figure 11 where the theoretical topography of continent–ocean distribution is described simply by a step function where the step is at the continent–ocean boundary. These lower spectra contain all the more stochastic distributions the higher the degree *n* is. For comparison the upper curve of each panel presents the observed total topography of the Earth which is essentially determined by the distribution of the continents and large islands like Greenland and Madagascar. The observed curve has been calculated from the coefficients given by *Lemoine et al.* [1998].

3.4. Variation of Parameters: Continental Evolution, Plateness, Other Features

[43] We varied the parameters *Ra* and σ_y to investigate the region in which we obtain Earth-like results and to find other regions characterized by different mechanisms. A multitude of runs were performed to convince us that the presented runs are by no means exceptional but representative of a significant portion of the parameter space. We find that the general character of these cases does not deviate too far from that of the real Earth. We compare the number, size, form and distribution of the calculated continents with the continent configuration of the present Earth. Solutions, which are Earth-like regarding the number and connectivity of continents, are shown by little black disks in the center of the $Ra-\sigma_y$ plot of Figure 12. *Ra* denotes the temporal average of the Rayleigh number of a given run. Figure 13 describes a quantitative measure of the deviation of the calculated present-time continental area from the observed one. Favorable agreement occurs in the center of the $Ra-\sigma_y$ plot. The corresponding runs are denoted by little black disks. Favorable in a generalized sense would mean that Earth-like solutions can be found in both Figures 12 and 13 in a common overlapping part of the $Ra-\sigma_y$ field. A classification of runs in terms of the planforms of flow near the surface is presented by Figure 14. Black disks denote plate-like solutions. An overlap set of the black disks is observed with the black disks of Figures 12 and 13. Figure 15 shows the distribution of classes of Urey numbers as a function of yield stress, σ_y, and time average of the Rayleigh number, *Ra*. Runs with realistic Urey numbers are

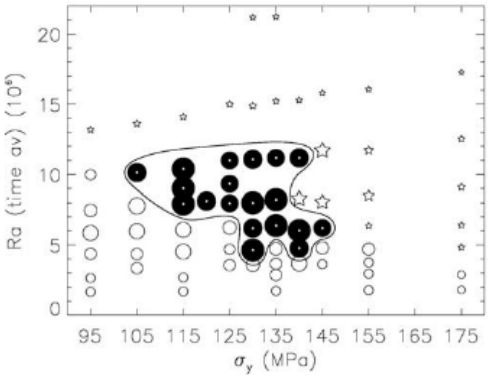

Figure 12. The types of continental distribution as a function of yield stress, σ_y, and of temporally averaged Rayleigh number, *Ra*. Each symbol of the plot denotes one run. Little black disks with a white center signify Earth-like distributions of the continents where the size of the disk is a measure of quality. The number of continents and its connectivity in relation to the observed ones are used as a measure of quality. Five-pointed stars stand for distributions with an unrealistic multitude of tiny continents. Open circles represent runs with reticularly connected, narrow stripe-like continents.

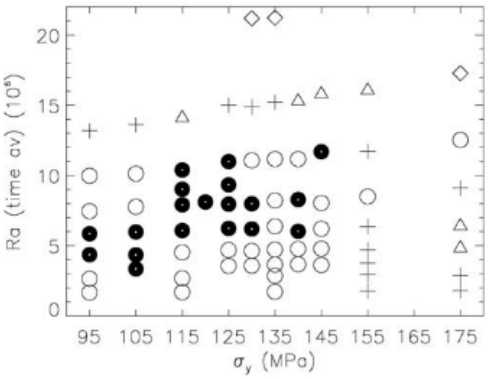

Figure 13. A classification of the runs with respect to the difference of observed surface percentage of continents (=40.35%) minus calculated surface percentage of continents. This difference, d_c, is plotted as a function of yield stress, σ_y, and of the time average of the Rayleigh number, *Ra*. Little black disks denote slight deviations, namely $-4.5 \leq d_c < 4.5$ percent. Open circles stand for $4.5 \leq d_c < 13.5$. Plus signs signify $13.5 \leq d_c < 22.5$. Open triangles represent runs with $22.5 \leq d_c < 31.5$. Open diamonds denote $31.5 \leq d_c < 40.5$.

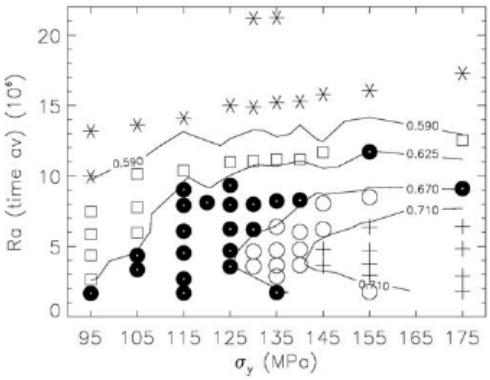

Figure 15. The time average of the Urey number, *Ur*, is plotted in a diagram the abscissa of which is the yield stress, σ_y, and the ordinate is the time average of the Rayleigh number, *Ra*. Asterisks represent runs with $Ur \leq 0.59$. Open squares signify $0.59 < Ur \leq 0.625$. Little black disks denote runs with $0.625 < Ur \leq 0.67$. Open circles depict runs with $0.67 < Ur \leq 0.71$. Finally, plus signs signify runs with $0.71 < Ur$.

represented by black disks. Using the abundances of potassium given in Table 3 and the mass of ^{40}Ar in the Earth's atmosphere, we estimate the ratio of the total heat production within the Earth to the total surface heat flow at 0.625 to 0.670. For comparison we remark that [*Schubert et al.*, 2001, p. 578] conclude that this Urey number is somewhere between 0.5 and 0.7. For a comparison of the present-time laterally averaged heat flows, *qob*(*now*), of the runs, it is important to filter away the random fluctuations. A simple

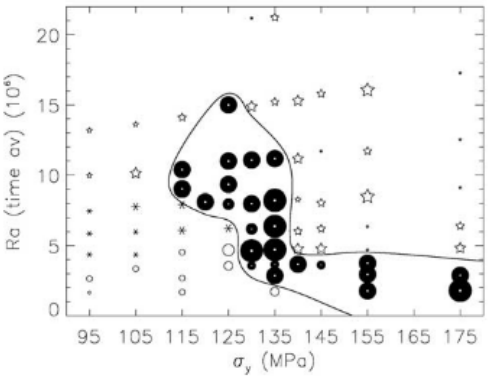

Figure 14. The types of lithospheric movements as a function of yield stress, σ_y, and time average of the Rayleigh number, *Ra*. Plate-like solutions with narrow subducting zones are depicted by little black disks. Its surface area is a measure of plateness. Open circles represent runs with broad downwellings and minor plateness. Open five-pointed stars denote unrealistic runs with local subduction only. Asterisks stand for rather complex planforms with lots of small but not narrow downwellings.

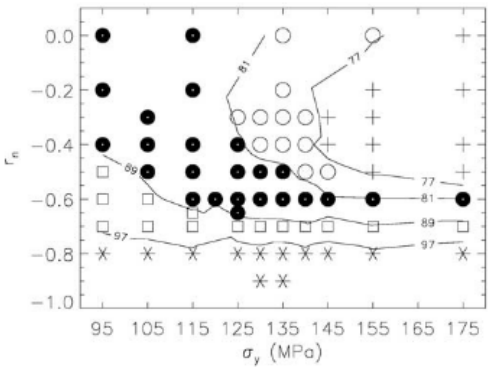

Figure 16. The symbols represent classes of the nonrandom values, *qob**, of the present-time surface average of the heat flow of the runs in a $r_n - \sigma_y$ plot where *qob** is calculated using equation (15). The following numbers are given in mW/m^2. Asterisks signify runs with $97 \leq qob^*$. Open squares depict runs with $89 \leq qob^* < 97$; little black disks stand for $81 \leq qob^* < 89$. Open circles denote runs with $77 \leq qob^* < 81$; plus signs represent the range $qob^* < 77$.

method to do so is to replace the calculated values of $qob(now)$ by qob^* where

$$qob^* = mean\left(\frac{qob(now)}{qob(time\ av)}\right) * qob(time\ av) \qquad (15)$$

The expression time *av* denotes the time average of one run, mean stands for the average of all runs of the plot. Figure 16 demonstrates the distribution of the filtered present-time surface average of the heat flow, qob^*, in an $r_n - \sigma_y$ diagram. Realistic values are again denoted by black disks. We observe a partial overlap with the favorable field of continent distribution of Figure 12.

4. General Discussion and Conclusions

[44] The problem of chemical differentiation of continental crust (CC) is very complex. CC is highly enriched in incompatible elements. Lead and large ion lithophile elements are strongly enriched relative to other trace elements. Thirdly, the existence of a phase is necessary which allows the fractionation of rare Earth elements [*Davidson and Arculus*, 2006]. The chemical similarity of average andesite and bulk CC prompted *Taylor* [1967] to introduce his andesite model. Ce/Pb and Nb/U fractionation seems to require a hydrous environment, probably a subduction zone rather than an OIB environment or plumes [*Arculus*, 1994]. However, there are at least five models for the origin of CC [*Davidson and Arculus*, 2006; *McLennan et al.*, 2006]. The episodic time distribution of CC formation obviously fits better to the episodicity of mantle plumes than to the continuous process of subduction. This and some geochemical arguments caused *Abbott et al.* [1997] and *Albarède* [1998] to propose that CC grows mainly by basaltic volcanism, especially oceanic plateau basalts, via mantle plumes. The pure Andean solution of the CC formation problem is now considered less probable since the Andean magmas are highly differentiated and better explained by the assumption that they are generated not only by extensive fractionation but also by contamination with preexisting CC. Any magma mixed with CC will look as though it was produced by subduction [*Arculus*, 1987; *Davidson and Arculus*, 2006]. *Parman* [2007] shows that the MORB contribution to CC generation dominates in the Phanerozoic while the OIB contribution prevails in the main preceding part of the mantle's evolution. This is the background for why we based our convection–fractionation model, particularly the geochemical part, on the more recently developed reservoir models by *Hofmann* [2003], *Stracke et al.* [2005], and *Willbold and Stracke* [2006] (cf. section 1.1). The abundances of the reservoirs of *McCulloch and Bennett* [1994] are similar to those ones given by *Hofmann* [2003].

[45] The essential content of this paper is a numerical convection–fractionation model with growing continents and, as a complement, a growing depleted MORB mantle. We obtained the following results. The laterally averaged present-day temperature profiles from our model fall between the profiles of standard parameterized models for whole mantle convection and for two-layered convection, but closer to the whole mantle curve (cf. Figure 8). Two typical viscosity profiles from our model are given by Figure 9. The derivation of it is to be found in *Walzer et al.* [2004a] where we also show that the existence of a prominent asthenosphere and a viscoplastic yield stress, σ_y, generates plate-like movements of pieces of oceanic lithosphere and elongated, narrow zones of subduction at the surface.

[46] *Rollinson* [2006] summarizes that there are three main views with respect to crustal growth through time: (1) CC increased at a linear rate from τ = 3.1 Ga to the present [*Hurley and Rand*, 1969]. (2) The full amount of CC developed at the beginning and has been recycled again and again [*Armstrong*, 1991]. We could supplement this view by the following question. Did the generation of the mass of CC exclusively take place at the beginning of the Earth's evolution as the generation of the crust of Moon and Mars was evidently connected with the quick chemical segregation in the first 200 Ma? (3) CC has grown progressively with time but in an episodic manner [*Condie*, 1998]. Figure 5 reveals that our model supports this third view.

[47] The Figures 6, 10, and 11 show that we obtain rather realistic distributions of continents applying only a few assumptions. We compare our results with the present distribution of the continents. Figure 12 defines a $Ra - \sigma_y$ area with realistic continent distributions but also regions with less realistic and irrelevant solutions. It is also noteworthy that even after 4.5 Ga, the reservoirs are not perfectly homogenized. Immediately beneath the lithosphere we find DMM (cf. Figure 6).

[48] Figures 3 and 4 demonstrate that the time evolution of the Rayleigh number, Ra_t, is surprisingly predictable from run to run as we smoothly vary the parameters. The laterally averaged surface heat flow, *qob*, diminishes slowly to the present-day value which is near the observed one (cf. Figure 7). The decrease of *qob* is considerably smaller than commonly found in parameterized models. This is a direct consequence of the assumed dependence of lithospheric viscosity on the abundances of volatiles. The corresponding reasoning is in section 3.3.

[49] A comparison of the Figures 12 to 16 shows the existence of a common $Ra - \sigma_y$ domain in which we obtain simultaneously realistic results for the following: Earth-like distribution of continents, difference between calculated present-time continental area and observed one, plateness, difference between the computed Urey number and the generally accepted value of it, difference between the calculated heat flow, qob^* and the observed heat flow. In future, we intend to develop the ability to include ridge differentiation that produces the MORB oceanic crust and the oceanic lithospheric mantle. At the beginning of this section, we explained why we did not do this already in this paper. We tested separately the individual steps of development of this model. An example for this has been given at the start of section 3.1. where we found a stable plate-like regime presupposed that there is a viscoplastic yield stress, σ_y, and an asthenosphere and that the $\sigma_y - r_n$ combination is in the plate-producing region of the $\sigma_y - r_n$ plot. This mechanism works with (cf. Figure 2) and without (cf. Figure 1) the chemical differentiation of oceanic plateaus plus continental growth.

Appendix A: The Tracer Method

[50] We use tracers to treat the movements of heat-producing elements. These movements arise from convec-

tion and differentiation. We assign a three-dimensional cell to each node in the icosahedral grid with 1351746 nodes. There are type-1 tracers, type-3 tracers and type-4 tracers with the abundances given in Table 3. At the beginning of the evolution of the model, the shell contains exclusively type-1 tracers. Each cell starts with eight tracers for basic runs (B-runs) or 64 tracers for comparative runs (C-runs). Each tracer represents not only a certain number of radioactive atoms or daughter nuclide atoms, respectively, but also the eighth (or 64th) part of the cell mass. The tracers are carried along by the velocity field. The element concentration of a node is determined by the mass-weighted mean, $\overline{a_{\mu\nu}}$, of the abundances of the elements carried by the tracers in the cell associated with the node.

A1. Conversion

[51] If the conditions for partial melting are fulfilled in a sufficiently large volume then the type-1 tracers in that volume are converted to type-4 tracers corresponding to DMM to mimic the depletion. A larger amount of changed Type-1 tracer mass is necessary to produce new Type-3 tracers (corresponding to CC) from Type-1 tracers near the surface above a region of differentiation, since the continental Type-3 tracers have considerably higher abundances of incompatible elements. Using the ratio, z_3, given by

$$z_3 = \left(a_{\mu\nu}^{(3)} - a_{\mu\nu}^{(1)}\right) / \left(a_{\mu\nu}^{(1)} - a_{\mu\nu}^{(4)}\right) \tag{A1}$$

the amounts of mass of incompatible elements are conserved during conversion.

[52] For uranium, z_3 = 67.13, based on the values of Table 3. Nearly the same ratio is obtained for thorium and potassium. So 67.13 type-1 tracer mass units from the asthenosphere are necessary to generate one type-3 tracer mass unit in the lithosphere by transformation of one type-1 tracer mass unit at the corresponding place. If a cell (1) has more than 50% type-1 tracer mass and is therefore fertile and (2) has fulfilled the condition $T > f_3 \times T_m$ in its grid point where f_3 is a fixed parameter with $0 < f_3 \leq 1$ and (3) has at least five neighboring cells with common boundary surfaces that also fulfill (1) and (2) then this cell is called type-A cell. If a cluster of simply connected type-A cells has a type-1 tracer mass *pm*4 with $pm4 \geq zthr$ then the tracers are instantaneously changed in type-4 tracers. Here *zthr* stands for the threshold mass. The center of gravity of the cluster is projected to the top surface of the shell. The corresponding point at the surface is called P'. A type-1 tracer mass $pm4/z3$ nearest to P' and not deeper than 65 km is changed to type-3 tracers. This corresponds to oceanic plateaus. All type-3 tracers are unsinkable and move with the horizontal component of the velocity field. This rule mimics the tendency of the continents to resist subduction.

A2. Formation of Continent

[53] If the mass percentage of the type-3 tracers goes beyond a prescribed value, expressed by *cmcrit*(= 0.6), inside a memory cell then they will be converted into continental tracers. Isolated terrane cells and continental cells contain at least one continental tracer. A terrane cell will be accreted to an existing continent if an additional thrust-fault condition is fulfilled. If the new, isolated terrane cell and a neighboring continental cell have a vector difference of their velocities such that they approach each other and if they finally touch then the terrane is joined to the continent.

A3. Continent Movement

[54] Tracers that are connected to form a continent move with a common angular velocity, ω, associated with that continent around the center of the shell. This quantity ω is calculated as the vector sum of the individual angular velocities derived from the horizontal components of the undisturbed nodal velocities. Hence the continent moves as a plate-like thin shell across the upper surface. In our present model, oceanic plates develop without any such constraints simply as a result of the yield stress and of the existence of an asthenosphere.

A4. Mantle Mass and Tracer Mass

[55] The sum of the individual particle masses is equal to the total mass of the mantle. The initial number of particles is called *npi*, therefore *npi* = 8 for B-runs and *npi* = 64 for C-runs. If, initially, the particles are regularly distributed to each cell then the mass, m_{ip}, of a tracer, *ip*, is calculated by

$$m_{ip} = (cell\ volume) * (nodal\ density)/(npi) \tag{A2}$$

The mass, M_{mantle}, of the whole mantle results from

$$M_{mantle} = \sum_{ip=1}^{npm} m_{ip} \tag{A3}$$

where *npm* is the total number of tracers in the mantle.

[56] A memory cell contains all tracers that are attributed to a node. Its base is a spherical hexagon or pentagon the corners of which are in the triangle centers of the triangular distribution around a node. Its altitude is again midway between the grid spherical surfaces *ir* and (*ir* + 1).

A5. Combining and Splitting

[57] Material from the top boundary layer that sinks to the CMB experiences a density increase and an increase of the tracer number per unit volume up to a factor two. However, the cell volume is diminished by a factor four during a movement from the surface to the CMB. So a reduction in the number of tracers per memory cell by a factor two is to be expected. If the tracer number falls below four (or 32) then each tracer of this cell is split into two tracers. The mass of such a tracer is distributed equally to the child tracers. The reverse process will occur during upwelling. Overcrowding of the memory cells can take place. For technical reasons, we limit the number of tracers per cell to 12 (or 96). Each tracer coming into the cell beyond this limit is combined with one of the other tracers according to their order in memory. Their masses are added. The location of the new tracer is the center of gravity of the two annihilated tracers. Only tracers of the same type can be combined. If an excess tracer enters the cell with a type not present in the cell, then two tracers of the most abundant type are united, the first two in the storage sequence. Splitting or combining does not alter the cell

accepted for publication in JOURNAL OF GEOPHYSICAL RESEARCH , 6 May 2008

mass, Mc, nor the sum of the tracer masses, m_{ipc}, present in the cell.

[58] The base of an interpolation cell, assigned to a node, is a spherical hexagon or pentagon the corners of which are the lateral neighboring nodes. The upper and lower bases are determined by the upper and lower neighboring grid spherical surfaces. All tracers inside the interpolation cell contribute to the interpolation of tracer attributes, e.g., elemental abundances, to the node. The nearer the tracer is to a grid point, the larger is the weighting factor. The lateral weighting factor, wl, is simply the barycentric coordinate of the tracer when the tracer and node are both radially projected onto the same spherical surface:

$$wl = (\alpha|\beta|\gamma)(ip) \tag{A4}$$

The radial weighting factor is given by

$$\begin{aligned} wr &= \frac{r_{ir+1} - r_{ip}}{r_{ir+1} - r_{ir}} \qquad if \quad r_{ip} > r_{ir} \\ wr &= \frac{r_{ip} - r_{ir-1}}{r_{ir} - r_{ir-1}} \qquad if \quad r_{ip} \le r_{ir} \end{aligned} \tag{A5}$$

where $r_{ir+1|ir-1}$ are the neighboring grid spherical surfaces of the radius, r_{ir}, of the node and r_{ip} is the radius of the tracer. The total weighting factor is the product of these two factors.

$$w_{ip} = wr * wl \tag{A6}$$

The weighted mass, wm_{ip}, of a tracer is

$$wm_{ip} = w_{ip} * m_{ip} \tag{A7}$$

[59] The mass, wMc, of an interpolation cell can be derived by a weighted integration over the mass continuum of the cell. This has to be done in such a way that

$$wMc(interpolation\,cell) = Mc(memory\,cell) \tag{A8}$$

[60] The total mass balance is not violated by the weighting procedure:

$$\begin{aligned} \sum_{c=1}^{nc}\sum_{ip=1}^{npc} wm_{ipc} &= \sum_{c=1}^{nc}\sum_{i3c=1}^{n3c}\sum_{ip3c=1}^{nip3c} wm_{ip3c} \\ &= \sum_{i3=1}^{n3}\sum_{ip3=1}^{nip3}\sum_{node=1}^{6} wm_{ip3,node} \\ &= \sum_{i3=1}^{n3}\sum_{ip3=1}^{nip3} (wr + (1-wr)) * (\alpha+\beta+\gamma) * m_{ip3} \\ &= \sum_{i3=1}^{n3}\sum_{ip3=1}^{nip3} m_{ip3} = \sum_{ip=1}^{np} m_{ip} \end{aligned} \tag{A9}$$

where n is a node number, c an interpolation cell, p a tracer, i counting index, 3 triangular cell, w weighted, m mass, $node$ the counting index for the nodes at the boundaries of a triangular cell, wr the radial weighting factor of a tracer; α, β, γ are the barycentric coordinates from the three corner points of the basis of a triangular cell, so that $\alpha + \beta + \gamma = 1$.

[61] A slight diminution of tracer mass can be observed in the spreading zones which is not induced by density differences. In other areas, a compaction of tracer mass is to be expected:

$$wMc \neq \sum_{ipc=1}^{npc} wm_{ipc} \tag{A10}$$

The tracer mass ratio, Gmc, of the cells deviates from the obligated value 1:

$$Gmc = \left(\sum_{ipc=1}^{npc} wm_{ipc}\right) / wMc \neq 1 \tag{A11}$$

This formula describes a distortion of the tracer representation. A local tracer mass refresh (LTR) has been introduced to reduce the discrepancy of equation (A11). We use LTR only if Gmc does not fulfill the condition $(Gmcmax)^{-1} \le Gmc \le Gmcmax$ where $Gmcmax = 50$. In the case of LTR, the cell c and its neighboring cells have to be united to a neighborhood cell cn. The new mass, $m'_{jp,k}$ of a tracer jp of the type k can be calculated by

$$m'_{jp,k} = \left[\sum_{icn=1}^{ncn}\sum_{ip=1}^{np_{icn}} m_{ip,k}\right] / np_k \tag{A12}$$

for $k = 1,3,4$ where np_k denotes the total number of type-k tracers in the neighborhood cell cn. The balance of each type of tracers is guaranteed in spite of LTR.

A6. Balance Test

[62] We calculate the time evolution of the heating error for each run to check the effect of the tracer conversion and the deviation

$$\sum_{ipc=1}^{npc} wm_{ipc} - wMc$$

This heating error is the relative difference between effective internal heating and internal heating of a corresponding homogeneous mantle. For example, the maximum heating error of run 816B is only 0.0055 for the whole mantle evolution and even only 0.0027 for 4500 $Ma \ge \tau \ge 1200$ Ma where τ is age.

Appendix B: Limitations of Terra and Future Improvements

[63] It is well known that the code Terra has some limitations, e.g., regarding viscosity variations. Therefore we started some special investigations [*Müller*, 2008; *Köstler*, 2009]. Furthermore, John Baumgardner is about to rewrite the code with a yin-yang grid. The following limitations and problems are treated and now partly solved by *Müller* [2008] and *Köstler* [2009].

[64] (1) Robustness of the multigrid algorithm. Although being very efficient with only $\mathcal{O}(n)$ operations needed for solving a linear equation system with n unknowns, the multigrid method is not easily applicable to systems with

strongly varying coefficients. In the algorithm we use, proposed by *Ramage and Wathen* [1994], the viscosity is the coefficient in the linear equation system we solve with multigrid. To represent such a varying coefficient on coarser grids accurately, *Yang* [1997] modified the code and implemented a matrix-dependent transfer technique. There with *Reese et al.* [2005] explored a parameter range of $\Delta\eta$ between 10^5 and 5×10^7 with an internal Rayleigh number of 10^6. Also, *Richards et al.* [2001] used this code to investigate surface mobility as a function of viscosity variation and yield stress. However, the viscosity profile derived in *Walzer et al.* [2004a] with three high-viscosity and three low-viscosity zones and steep gradients is very challenging to be represented properly on coarser grids [*Müller*, 2008]. Here we are going to improve the matrix-dependent transfer technique to transfer these high and low peaks to the coarsest grid possible. Moreover, we try to implement state-of-the-art conjugate gradient solvers (i.e., preconditioned MINRES) into the solving routines in Terra.

[65] (2) Advection and time stepping. The MPDATA scheme [*Bunge and Baumgardner*, 1995] is used for the solution of the energy equation. This is still common in the community. However, because of its numerical diffusion, investigation of an improved time stepping scheme is planned for future research.

[66] (3) Benchmarks. With Terra there exists a lack of validation of the numerical model. Although benchmarks for tetrahedral steady state solutions are given at $Ra = 7000$ and $Ra = 14{,}000$ by *Richards et al.* [2001], these apply only for constant viscosity. Hence we plan efforts to publish results of test cases which were used by *Stemmer et al.* [2006] to compare different mantle convection models with each other. These cases include weakly temperature-dependent viscosity for steady state solutions at $Ra = 7000$ and $Ra = 14{,}000$ and strongly temperature-dependent viscosity for weakly time-dependent flow at $Ra = 10^5$.

[67] *Müller* [2008] found the following improvements regarding the pressure instability. The time discretization of Terra produces a series of compressible Stokes problems. This does not mean that the present pressure solution has spurious oscillations but in this case it is necessary to show that a stabilization scheme works well. Using an approximation, the compressible Stokes problems are transformed to saddle point problems that are equivalent to the standard incompressible Stokes problem in different variables. It is however well known that the pressure solution for the incompressible Stokes problem is unstable unless the Ladyzhenskaya–Babuska–Brezzi condition (LBB) is satisfied by the discretization, resulting in a vector space of spurious pressure modes that are not detectable by the discretization. If such pressure defects arise, the solver is not able to correct them since they are invisible to it. At least for one particular Stokes problem, the velocity solution is not tainted. For the mentioned series of Stokes problems even this is not true. This can be proven as follows. The artificial pressure field in the current time step produces an artificial viscosity field for the next time step due to the pressure dependence of the viscosity. The viscosity fields in turn affect the momentum operators that are used to obtain the solutions for the velocity. It is now clear that the code has to fulfill the LBB. Unfortunately, the equal-order discretization of the original Terra does not fulfill the LBB and suffers therefore from the mentioned difficulties. The problem is further increased by the introduction of local grid refinements with hanging nodes. Therefore the discretization has been modified in a simple way so that the LBB holds even in the presence of hanging nodes. The key idea is to use a pressure grid featuring twice the mesh width of the velocity. The stability can be proven for macroelements and thus for the whole discretization.

[68] In Terra, the Stokes problems are solved using a Schur complement approach. This algorithm demands the action of the inverse of the momentum operator $\nabla \cdot \tau$ on the viscosity field where τ is the deviatoric stress tensor. The action of the inverse is approximated by a multigrid algorithm. The essence of this algorithm is the representation of the problem on coarser grids to estimate the desired solution on the finest grid. Grid refinement is an extraordinary important task since at the mantle phase boundaries not only the density and the seismic velocities but also the activation energies and volumes will jump. Therefore essential viscosity steps are to be expected there [*Walzer et al.*, 2004a]. That is, why *Müller* [2008] treated the following three partial problems.

[69] (4) Intergrid transfer. A solution on the coarse grid must be prolongated to the fine grid. This is usually done by extrapolation which often means to compute mean values for fine grid points not included in the coarse grid. So a kind of smooth fine grid estimate is achieved. However, this procedure can be incorrect if the fine grid solution is not smooth in the above mentioned sense. Unfortunately this is what happens in the case of viscosity jumps. The transfer to the finer grid introduces a mean value for the velocity where it should be either high or low. Since Terra uses a Galerkin intergrid transfer, the operators for prolongation and restriction are strictly coupled so that only one of them can be chosen arbitrarily. So we can look at the problem also from the opposite point of view, namely from restriction. If we want to approximate a discontinuous viscosity distribution on the fine grid, we have to preserve this very discontinuity on the coarse mesh, i.e., we must not smear the coarse-grid velocity field. So what we have to do is a sort of injection instead of the usual interpolation. Due to the Galerkin method, the coarse grid operator is also defined purely mathematically by either restriction or prolongation. Nevertheless, we can still assume a certain physical relevance. This can be seen if we ask from what kind of viscosity field the coarse grid operator would be induced if it was gained by discretization on the coarse mesh. This fact leads us to the following additional restriction.

[70] (5) Coarse-grid mesh width. Clearly, the multigrid idea works only if the coarse-grid representation of the operator is trustworthy. This cannot be true if the coarse grid is too coarse to resolve the coefficient discontinuities. In our case, the smallest wavelength of the viscosity variation is a natural boundary for the mesh size of any reasonable coarse grid. We address this issue by a kind of stopping criterion for the coarsening process as well as by local grid refinement.

[71] (6) Smoothing. Due to the parallelization of the smoothing process, the original Terra uses a radial block-Jacobi method rather than the slightly more effective Gauss–Seidel algorithm. The blocking is necessary since the original Jacobi requires strict diagonal dominance of the

operator to converge. This dominance is not the case for varying viscosity. The blocking can be interpreted as a coupling of neighboring nodes during the smoothing process. In the present model, we assume that the viscosity varies mostly in radial direction. Therefore the choice of blocking in Terra is natural. This also explains the lack of capacity to handle lateral viscosity variations. Of course, a lateral blocking would be much more effective for lateral variations. This suggests a kind of blocking in all directions. However, even if we adopt such a blocking scheme it is possible to construct a viscosity field the smoother cannot handle. This is due to the fact that, also for neighboring nodes of different blocks, couplings exist that are not taken into account. An often proposed procedure is the use of adaptive blocking to include at least the strongest dependencies in the block. Since this would destroy the load balancing of our parallelization, *Müller* [2008] has looked for and found another solution which is robust against nearly arbitrary parameter discontinuities. He combines different block decompositions of the unknowns, thus catching every parameter jump in a block of at least one decomposition. Two-dimensional test problems show the superiority of this idea. Therefore we intend to implement it.

[72] **Acknowledgments.** We kindly acknowledge the confidential cooperation of many years' standing with John Baumgardner, who gave many excellent pieces of advice. We gratefully acknowledge the help of Dave Stegman. He provided us with his particle code and discussed some problems with us. Ctirad Matyska and two anonymous reviewers provided very useful comments on an earlier version of this paper. We also thank Peter Lammers (HLRS) for his kind advice concerning the adaptation of the code to the available platform.

[73] This work was partly supported by the Deutsche Forschungsgemeinschaft under grant WA 1035/5-3. We acknowledge the use of supercomputing facilities at LRZ München, HLRS Stuttgart, and NIC Jülich.

References

Abbott, D. H., L. Burgess, and J. Longhi (1994), An empirical thermal history of the Earth's upper mantle, *J. Geophys. Res.*, *99*, 13,835–13,850.

Abbott, D. H., R. Drury, and W. D. Mooney (1997), Continents as lithological icebergs: The importance of buoyant lithospheric roots, *Earth Planet. Sci. Lett.*, *149*, 15–27.

Albarède, F. (1998), The growth of continental crust, *Tectonophysics*, *296*, 1–14.

Allègre, C. J. (2002), The evolution of mantle mixing, *Philos. Trans. R. Soc. A: Math. Phys. Eng. Sci.*, *360*, 2411–2431.

Allègre, C. J., and E. Levin (1995), Isotopic systems and stirring times of the Earth's mantle, *Earth Planet. Sci. Lett.*, *136*, 629–646.

Arculus, R. J. (1987), The significance of source versus process in the tectonic controls of magma genesis, *J. Volcanol. Geotherm. Res.*, *32*, 1–12.

Arculus, R. J. (1994), Aspects of magma genesis in arcs, *Lithos*, *33*, 189–208.

Arculus, R. J., H. Lapierre, and É. Jaillard (1999), Geochemical window into subduction and accretion processes: Raspas metamorphic complex, Ecuador, *Geology*, *27*(6), 547–550.

Armstrong, R. L. (1991), The persistent myth of crustal growth, *Aust. J. Earth Sci.*, *38*, 613–640.

Baumgardner, J. R. (1983), A three-dimensional finite element model for mantle convection, Ph.D. thesis, Univ. of California, Los Angeles, Calif.

Bennett, V. C. (2003), Compositional evolution of the mantle, in *Treatise on Geochemistry, Vol. 2: The Mantle and the Core*, edited by R. W. Carlson, pp. 493–519, Elsevier, Amsterdam.

Bercovici, D. (1996), Plate generation in a simple model of lithosphere-mantle flow with dynamic self-lubrication, *Earth Planet. Sci. Lett.*, *144*, 41–51.

Bercovici, D. (1998), Generation of plate tectonics from lithosphere-mantle flow and void-volatile self-lubrication, *Earth Planet. Sci. Lett.*, *154*, 139–151.

Bercovici, D. (2003), The generation of plate tectonics from mantle convection, *Earth Planet. Sci. Lett.*, *205*, 107–121.

Bercovici, D., and S.-I. Karato (2003), Whole-mantle convection and the transition-zone water filter, *Nature*, *425*, 39–44.

Bowring, S. A., and T. Housh (1995), The Earth's early evolution, *Science*, *269*, 1535–1540.

Brown, M., and T. Rushmer (Eds.) (2006), *Evolution and Differentiation of the Continental Crust*, Cambridge Univ. Press, Cambridge, U.K.

Buffett, B. A., H. E. Huppert, J. R. Lister, and A. W. Woods (1996), On the thermal evolution of the Earth's core, *J. Geophys. Res.*, *101*, 7989–8006.

Bunge, H.-P. (1996), Global mantle convection models, Ph.D. thesis, UC Berkeley, Calif.

Bunge, H.-P., and J. R. Baumgardner (1995), Mantle convection modelling on parallel virtual machines, *Comput. Phys.*, *9*, 207–215.

Bunge, H.-P., and M. A. Richards (1996), The origin of long-wavelength structure in mantle convection, *Geophys. Res. Lett.*, *23*, 2987–2990.

Bunge, H.-P., M. A. Richards, and J. R. Baumgardner (1997), A sensitivity study of three-dimensional spherical mantle convection at 10^8 Rayleigh number: Effects of depth-dependent viscosity, heating mode and an endothermic phase change, *J. Geophys. Res.*, *102*, 11,991–12,007.

Christensen, U. R. (1984), Heat transport by variable viscosity convection and implications for the Earth's thermal evolution, *Phys. Earth Planet. Int.*, *35*, 264–282.

Christensen, U. R. (1985a), Heat transport by variable viscosity convection: II. Pressure influence, non-Newtonian rheology and decaying heat sources, *Phys. Earth Planet. Int.*, *37*, 183–205.

Christensen, U. R. (1985b), Thermal evolution models for the Earth, *J. Geophys. Res.*, *90*, 2995–3007.

Christensen, U., and H. Harder (1991), Three-dimensional convection with variable viscosity, *Geophys. J. Int.*, *104*, 213–226.

Christensen, U. R., and A. W. Hofmann (1994), Segregation of subducted oceanic crust in the convecting mantle, *J. Geophys. Res.*, *99*, 19,867–19,884.

Coffin, M. F., and O. Eldholm (1994), Large igneous provinces: Crustal structure, dimensions and external consequences, *Rev. Geophys.*, *32*, 1–36.

Coltice, N., B. R. Phillips, H. Bertrand, Y. Ricard, and P. Rey (2007), Global warming of the mantle at the origin of flood basalts over supercontinents, *Geology*, *35*, 391–394.

Condie, K. C. (1998), Episodic continental growth and supercontinents: A mantle avalanche connection?, *Earth Planet. Sci. Lett.*, *163*, 97–108.

Condie, K. C. (2000), Episodic continental growth models: Afterthoughts and extensions, *Tectonophysics*, *322*, 153–162.

Cserepes, L., D. A. Yuen, and B. A. Schroeder (2000), Effect of the mid-mantle viscosity and phase-transition structure on 3D mantle convection, *Phys. Earth Planet. Int.*, *118*, 135–148.

Davidson, J. P., and R. J. Arculus (2006), The significance of Phanerozoic arc magmatism in generating continental crust, in *Evolution and Differentiation of the Continental Crust*, edited by M. Brown and T. Rushmer, pp. 135–172, Cambridge Univ. Press, Cambridge, U.K.

Davies, G. F. (2002), Stirring geochemistry in mantle convection models with stiff plates and slabs, *Geochim. Cosmochim. Acta*, *66*(17), 3125–3142.

Davies, G. F. (2006), Gravitational depletion of the early Earth's upper mantle and the viability of early plate tectonics, *Earth Planet. Sci. Lett.*, *243*, 376–382.

Dziewonski, A. M., and D. L. Anderson (1981), Preliminary reference Earth model, *Phys. Earth Planet. Int.*, *25*, 297–356.

Fei, Y., C. M. Bertka, and B. O. Mysen (Eds.) (1999), *Mantle Petrology: Field Observations and High-Pressure Experimentation: A Tribute to Francis R. (Joe) Boyd*, *Spec. Publ. Geochem. Soc.*, vol. 6, 322 pp., Geochem. Soc., Houston, TX.

Fisher, R. V., and H. U. Schmincke (1984), *Pyroclastic Rocks*, Springer, Berlin.

Forte, A. M., and J. X. Mitrovica (2001), Deep-mantle high-viscosity flow and thermochemical structure inferred from seismic and geodynamic data, *Nature*, *410*, 1049–1056.

Fowler, C. M. R., C. J. Ebinger, and C. J. Hawkesworth (Eds.) (2002), *The Early Earth: Physical, Chemical and Biological Development*, *GSL Spec. Publ.*, vol. 199, 352 pp., Geol. Soc., Houston, Tx.

Frost, D. J. (2006), The stability of hydrous mantle phases, *Rev. Min. Geochem.*, *62*, 243–271.

Gable, C. W., R. J. O'Connell, and B. J. Travis (1991), Convection in three dimensions with surface plates: Generation of toroidal flow, *J. Geophys. Res.*, *96*, 8391–8405.

Gallavotti, G. (2002), *Foundations of Fluid Dynamics*, 510 pp., Springer, Berlin.

Gilvarry, J. J. (1956), The Lindemann and Grüneisen laws, *Phys. Rev.*, *102*, 307–316.

Glatzmaier, G. A. (1988), Numerical simulations of mantle convection: Time-dependent, three-dimensional, compressible, spherical shell, *Geophys. Astrophys. Fluid Dyn.*, *43*, 223–264.

Green, D. H., and T. J. Falloon (1998), Pyrolite: A Ringwood concept and its current expression, in *The Earth's Mantle. Composition, Structure and Evolution*, edited by I. Jackson, pp. 311–378, Cambridge Univ. Press, Cambridge, U.K.

Grove, T. L., and S. W. Parman (2004), Thermal evolution of the Earth as recorded by komatiites, *Earth Planet. Sci. Lett.*, *219*, 173–187.

Grove, T. L., N. Chatterjee, S. W. Parman, and E. Medard (2006), The influence of H_2O on mantle wedge melting, *Earth Planet. Sci. Lett.*, *249*, 74–89.

Gurnis, M. (1988), Large-scale mantle convection and the aggregation and dispersal of supercontinents, *Nature*, *332*, 695–699.

Hager, B. H., and R. J. O'Connell (1981), A simple global model of plate dynamics and mantle convection, *J. Geophys. Res.*, *86*, 4843–4867.

Hansen, U., and D. A. Yuen (1993), High Rayleigh number regime of temperature-dependent viscosity convection and the Earth's early thermal history, *Geophys. Res. Lett.*, *20*, 2191–2194.

Hart, S. R., E. H. Hauri, L. A. Oschmann, and J. A. Whitehead (1992), Mantle plumes and entrainment: Isotopic evidence, *Science*, *256*, 517–520.

Hawkesworth, C. J., and A. I. S. Kemp (2006), The differentiation and rates of generation of the continental crust, *Chem. Geol.*, *266*, 134–143.

Heier, K. S. (1978), The distribution and redistribution of heat-producing elements in the continents, *Philos. Trans. R. Soc. A: Math. Phys. Eng. Sci.*, *288*, 393–400.

Hirschmann, M. M., C. Aubaud, and A. C. Withers (2005), Storage capacity of H_2O in nominally anhydrous minerals in the upper mantle, *Earth Planet. Sci. Lett.*, *236*, 167–181.

Hirth, G. (2006), Protons lead the charge, *Nature*, *443*, 927–928.

Hofmann, A. W. (1988), Chemical differentiation of the Earth: The relationship between mantle, continental crust and oceanic crust, *Earth Planet. Sci. Lett.*, *90*, 297–314.

Hofmann, A. W. (2003), Sampling mantle heterogeneity through oceanic basalts: Isotopes and trace elements, in *Treatise on Geochemistry, Vol. 2: The Mantle and the Core*, edited by R. W. Carlson, pp. 61–101, Elsevier, Amsterdam.

Honda, S., and Y. Iwase (1996), Comparison of the dynamic and parameterized models of mantle convection including core cooling, *Earth Planet. Sci. Lett.*, *139*, 133–145.

Howell, D. G. (1989), *Tectonics of Suspect Terranes: Mountain Building and Continental Growth*, CRC Press, New York.

Hurley, P. M., and J. R. Rand (1969), Pre-drift continental nuclei, *Science*, *164*, 1229–1242.

Jochum, K. P., A. W. Hofmann, E. Ito, H. M. Seufert, and W. M. White (1983), K, U and Th in mid-ocean ridge basalt glasses and heat production, K/U and K/Rb in the mantle, *Nature*, *306*, 431–436.

Jones, A. G., R. W. Carlson, and H. Grutter (Eds.) (2004), *A Tale of Two Cratons: The Slave-Kaapvaal Workshop*, 504 pp., Elsevier, Amsterdam.

Kameyama, M., and M. Ogawa (2000), Transitions in thermal convection with strongly temperature-dependent viscosity in a wide box, *Earth Planet. Sci. Lett.*, *180*, 355–367.

Karato, S.-I. (1997), Phase transformations and rheological properties of mantle minerals, in *Earth's Deep Interior*, edited by D. Crossley, pp. 223–272, Gordon and Breach Sci. Publ., New York.

Karato, S.-I., and P. Li (1992), Diffusion creep in perovskite: Implications for the rheology of the lower mantle, *Science*, *255*, 1238–1240.

Karato, S.-I., and P. Wu (1993), Rheology of the upper mantle: A synthesis, *Science*, *260*, 771–778.

Karato, S.-I., Z. Wang, B. Liu, and K. Fujino (1995), Plastic deformation of garnets: Systematics and implications for the rheology of the mantle transition zone, *Earth Planet. Sci. Lett.*, *130*, 13–30.

Kemp, A. I. S., C. J. Hawkesworth, B. A. Paterson, and P. D. Kinny (2006), Episodic growth of the Gondwana supercontinent from hafnium and oxygen isotopes in zircon, *Nature*, *439*, 580–583.

Keppler, H., and N. Bolfan-Casanova (2006), Thermodynamics of water solubility and partitioning, *Rev. Min. Geochem.*, *62*, 193–230.

Kido, M., and O. Cadek (1997), Inferences of viscosity from the oceanic geoid: indication of a low viscosity zone below the 660-km discontinuity, *Earth Planet. Sci. Lett.*, *151*, 125–137.

Kido, M., D. A. Yuen, O. Cadek, and T. Nakakuki (1998), Mantle viscosity derived by genetic algorithm using oceanic geoid and seismic tomography for whole-mantle versus blocked-flow situations, *Phys. Earth Planet. Int.*, *107*, 307–326.

Kohlstedt, D., B. Evans, and S. Mackwell (1995), Strength of the lithosphere: Constraints imposed by laboratory experiments, *J. Geophys. Res.*, *100*, 17,587–17,602.

Komiya, T. (2004), Material circulation model including chemical differentiation within the mantle and secular variation of temperature and composition of the mantle, *Phys. Earth Planet. Int.*, *146*, 333–367.

Köstler, C. (2009), Iterative solvers for modeling mantle convection with strongly varying viscosity, Ph.D. thesis, Friedrich-Schiller Univ. Jena, Germany.

Kramers, J. D., and I. N. Tolstikhin (1997), Two terrestrial lead isotope paradoxes, forward transport modelling, core formation and the history of the continental crust, *Chem. Geol.*, *139*, 75–110.

Lemoine, F. G., et al. (1998), The Development of the Joint NASA GSFC and the NIMA Geopotential Model EGM96, *NASA Goddard Space Flight Center*, *NASA/TP-1998-206861*, 575 pp.

Lenardic, A., L.-N. Moresi, and H. Mühlhaus (2003), Longevity and stability of cratonic lithosphere: Insights from numerical simulations of coupled mantle convection and continental tectonics, *J. Geophys. Res.*, *108*(B6), 2306, doi:10.1029/2002JB001859.

Lenardic, A., L.-N. Moresi, A. M. Jellinek, and M. Manga (2005), Continental insulation, mantle cooling, and the surface area of oceans and continents, *Earth Planet. Sci. Lett.*, *234*, 317–333.

Li, P., S.-I. Karato, and Z. Wang (1996), High-temperature creep in fine-grained polycristalline $CaTiO_3$, an analogue material of (Mg, Fe)SiO_3 perovskite, *Phys. Earth Planet. Int.*, *95*, 19–36.

Lowman, J. P., and G. T. Jarvis (1996), Continental collisions in wide aspect ratio and high Rayleigh number two-dimensional mantle convection models, *J. Geophys. Res.*, *101*, 25,485–25,497.

Matyska, C., and D. A. Yuen (2005), The importance of radiative heat transfer on superplumes in the lower mantle with the new post-perovskite phase change, *Earth Planet. Sci. Lett.*, *234*, 71–81.

Matyska, C., and D. A. Yuen (2006), Lower mantle dynamics with the post-perovskite phase change, radiative thermal conductivity, temperature- and depth-dependent viscosity, *Phys. Earth Planet. Int.*, *154*, 196–207.

McCulloch, M. T., and V. C. Bennett (1994), Progressive growth of the Earth's continental crust and depleted mantle: Geochemical constraints, *Geochim. Cosmochim. Acta*, *58*, 4717–4738.

McLennan, S. M., S. R. Taylor, S. R. Hemming (2006), Composition, differentiation, and evolution of continental crust: constraints from sedimentary rocks and heat flow, in *Evolution and Differentiation of the Continental Crust*, edited by M. Brown and T. Rushmer, pp. 92–134, Cambridge Univ. Press, Cambridge, U.K.

Meade, C., and R. Jeanloz (1990), The strength of mantle silicates at high pressures and room temperature: Implications for the viscosity of the mantle, *Nature*, *348*, 533–535.

Mei, S., and D. L. Kohlstedt (2000), Influence of water on plastic deformation of olivine aggregates 2. Dislocation creep regime, *J. Geophys. Res.*, *105*, 21,471–21,481.

Mierdel, K. (2006), Wasserlöslichkeit in Enstatit, Ph.D. thesis, Univ. Tübingen, 105 pp., Tübingen, Germany.

Mierdel, K., H. Keppler, J. R. Smyth, and F. Langenhorst (2007), Water solubility in aluminous orthopyroxene and the origin of the Earth's asthenosphere, *Science*, *315*, 364–368.

Monin, A. S. (1990), *Theoretical Geophysical Fluid Dynamics*, 399 pp., Kluwer Acad. Publ., Dordrecht.

Monnereau, M., and S. Quéré (2001), Spherical shell models of mantle convection with tectonic plates, *Earth Planet. Sci. Lett.*, *184*, 575–587.

Moresi, L.-N., and V. S. Solomatov (1995), Numerical investigation of 2D convection with extremely large viscosity variations, *Phys. Fluids*, *7*, 2154–2162.

Müller, M. (2008), Toward a robust Terra code, Ph.D. thesis, Friedrich-Schiller Univ. Jena, Germany.

Nagler, T. F., and J. D. Kramers (1998), Nd isotopic evolution of the upper mantle during the Precambrian: Models, data and the uncertainty of both, *Precambr. Res.*, *91*, 233–253.

Nisbet, E. G., M. J. Cheadle, N. T. Arndt, and M. J. Bickle (1993), Constraining the potential temperature of the Archean mantle: A review of the evidence from komatiites, *Lithos*, *30*, 291–307.

Ogawa, M. (1993), A numerical model of coupled magmatism-mantle convection system in Venus and the Earth's mantle beneath Archean continental crusts, *Icarus*, *102*(1), 40–61.

Ogawa, M. (1994), Effects of chemical fractionation of heat-producing elements on mantle evolution inferred from a numerical model of coupled magmatism-mantle convection system, *Phys. Earth Planet. Int.*, *83*(2), 101–127.

Ogawa, M. (1997), A bifurcation in the coupled magmatism-mantle convection system and its implications for the evolution of the Earth's upper mantle, *Phys. Earth Planet. Int.*, *102*, 259–276.

Ogawa, M. (2000), Coupled magmatism-mantle convection system with variable viscosity, *Tectonophysics*, *32*, 1–18.

Ogawa, M. (2003a), Plate-like regime of a numerically modeled thermal convection in a fluid with temperature-, pressure-, and stress-history-dependent viscosity, *J. Geophys. Res.*, *108*(B2), 2067, doi:10.1029/2000JB000069.

Ogawa, M. (2003b), Chemical stratification in a two-dimensional convecting mantle with magmatism and moving plates, *J. Geophys. Res.*, *108*(B12), 2561, doi:10.1029/2002JB002205.

Ogawa, M. (2008), Mantle convection: A review, *Fluid Dyn. Res.*, doi:10.1016/j.fluiddyn.2007.09.001.

accepted for publication in JOURNAL OF GEOPHYSICAL RESEARCH , 6 May 2008

Ogawa, M., G. Schubert, and A. Zebib (1991), Numerical simulations of three-dimensional thermal convection in a fluid with strongly temperature-dependent viscosity, *J. Fluid Mech.*, *233*, 299–328.
Palme, H., and H. S. C. O'Neill (2003), Cosmochemical estimates of mantle composition, in *Treatise on Geochemistry, Vol. 2*: *The Mantle and the Core*, edited by R. W. Carlson, pp. 1–38, Elsevier, Amsterdam.
Parman, S. W. (2007), Helium isotopic evidence for episodic mantle melting and crustal growth, *Nature*, *446*, 900–903.
Parman, S. W., J. C. Dann, T. L. Grove, and M. J. de Wit (1997), Emplacement conditions of komatiite magmas from the 3.49 Ga Komati Formation, Barberton Greenstone Belt, South Africa, *Earth Planet. Sci. Lett.*, *150*, 303–323.
Phillips, B. R., and H.-P. Bunge (2005), Heterogeneity and time dependence in 3D spherical mantle convection with continental drift, *Earth Planet. Sci. Lett.*, *233*, 121–135.
Pollak, H. N., S. J. Hurter, and J. R. Johnson (1993), Heat flow from the Earth's interior: Analysis of the global data set, *Rev. Geophys.*, *31*, 267–280.
Porcelli, D., and C. J. Ballentine (2002), Models for the distribution of terrestrial noble gases and evolution of the atmosphere, in *Noble Gases in Geochemistry and Cosmochemistry, Rev. Min. Geochem.*, vol. 47, edited by D. Porcelli, C. J. Ballentine, and R. Wieler, pp. 411–480, Mineral. Soc. of Am., Washington, D. C.
Ramage, A., and A. J. Wathen (1994), Iterative solution techniques for the Stokes and the Navier-Stokes equations, *Int. J. Numer. Methods Fluids*, *19*, 67–83.
Reese, C. C., V. S. Solomatov, and J. R. Baumgardner (2005), Scaling laws for time-dependent stagnant lid convection in a spherical shell, *Phys. Earth Planet. Int.*, *149*, 361–370.
Regenauer-Lieb, K., D. A. Yuen, and J. Branlund (2001), The initiation of subduction: Criticality by addition of water?, *Science*, *294*, 578–580.
Richards, M. A., W.-S. Yang, J. R. Baumgardner, and H.-P. Bunge (2001), Role of a low-viscosity zone in stabilizing plate tectonics: Implications for comparative terrestrial planetology, *Geochem. Geophys. Geosyst.*, *3*, 1040, doi:10.1029/2000GC000115.
Richter, F. M. (1973), Finite amplitude convection through a phase boundary, *Geophys. J. R. Astron. Soc.*, *35*, 265–276.
Rollinson, H. (2006), Crustal generation in the Archean, in *Evolution and Differentiation of the Continental Crust*, edited by M. Brown and T. Rushmer, pp. 173–230, Cambridge Univ. Press, Cambridge, U.K.
Rudnick, R. L., and D. M. Fountain (1995), Nature and composition of the continental crust: A lower crustal perspective, *Rev. Geophys.*, *33*, 267–309.
Schmeling, H. (2006), A model of episodic melt extraction for plumes, *J. Geophys. Res.*, *111*, B03202, doi:10.1029/2004JB003423.
Schubert, G., D. L. Turcotte, and T. R. Olson (2001), *Mantle Convection in the Earth and Planets*, Cambridge Univ. Press, Cambridge, U.K.
Sidorin, I., and M. Gurnis (1998), Geodynamically consistent seismic velocity predictions at the base of the mantle, in *The Core-Mantle Boundary Region, Geodyn. Ser.*, vol. 28, edited by M. Gurnis et al., pp. 209–230, AGU, Washington, D. C.
Sleep, N. H. (2005), Evolution of the continental lithosphere, *Annu. Rev. Earth Planet Sci.*, *33*, 369–393.
Solomatov, V. S. (1995), Scaling of temperature- and stress-dependent viscosity convection, *Phys. Fluids*, *7*, 266–274.
Stein, C., J. Schmalzl, and U. Hansen (2004), The effect of rheological parameters on plate behavior in a self-consistent model of mantle convection, *Phys. Earth Planet. Int.*, *142*, 225–255.
Steinbach, V., and D. A. Yuen (1994), Effects of depth-dependent properties on thermal anomalies produced in flush instabilities from phase transitions, *Phys. Earth Planet. Int.*, *86*, 165–183.
Steinbach, V., D. A. Yuen, and W. L. Zhao (1993), Instabilities from phase transitions and the timescales of mantle thermal convection, *Geophys. Res. Lett.*, *20*, 1119–1122.
Stemmer, K., H. Harder, and U. Hansen (2006), A new method to simulate convection with strongly temperature- and pressure-dependent viscosity in a spherical shell: Applications to the Earth's mantle, *Phys. Earth Planet. Int.*, *157*, 223–249.
Stracke, A., A. W. Hofmann, and S. R. Hart (2005), FOZO, HIMU and the rest of the mantle zoo, *Geochem. Geophys. Geosyst.*, *6*, Q05007, doi:10.1029/2004GC000824.
Tackley, P. J. (1993), Effects of strongly temperature-dependent viscosity on time-dependent, three-dimensional models of mantle convection, *Geophys. Res. Lett.*, *20*, 2187–2190.
Tackley, P. J. (2000a), Self-consistent generation of tectonic plates in time-dependent, three-dimensional mantle convection simulations: Part 1. Pseudoplastic yielding, *Geochem. Geophys. Geosyst.*, *1*, doi:10.1029/2000GC000036.
Tackley, P. J. (2000b), Self-consistent generation of tectonic plates in time-dependent, three-dimensional mantle convection simulations: Part 2. Strain weakening and asthenosphere, *Geochem. Geophys. Geosyst.*, *1*, doi:10.1029/2000GC000043.
Tackley, P. J. (2000c), Mantle convection and plate tectonics: Towards an integrated physical and chemical theory, *Science*, *288*, 2002–2007.
Takahashi, E. (1990), Speculations on the Archean mantle: Missing link between komatiite and depleted garnet peridotite, *J. Geophys. Res.*, *95*, 15,941–15,954.
Taylor, S. R. (1967), The origin and growth of continents, *Tectonophysics*, *4*, 17–34.
Taylor, S. R., and S. M. McLennan (1985), *The Continental Crust: Its Composition and Evolution*, Blackwell Scientific, Oxford.
Taylor, S. R., and S. M. McLennan (1995), The geochemical evolution of the continental crust, *Rev. Geophys.*, *33*, 241–265.
Tozer, D. C. (1967), Towards a therory of thermal convection in the mantle, in *The Earth's Mantle*, edited by T. Gaskell, pp. 325–353, Academic Press, London.
Trompert, R., and U. Hansen (1998), Mantle convection simulations with rheologies that generate plate-like behavior, *Nature*, *395*, 686–689.
van der Hilst, R. D., and W. F. McDonough (Eds.) (1999), *Composition, Deep Structure and Evolution of Continents*, 342 pp., Elsevier, Amsterdam.
Vashchenko, V. I. A., and V. N. Zubarev (1963), Free volume theory used to derive an expression for the Grüneisen constant gamma, including an analysis of the degree of approximation, *Sov. Phys. Solid State*, *5*, 653–655.
Walzer, U., and R. Hendel (1999), A new convection-fractionation model for the evolution of the principal geochemical reservoirs of the Earth's mantle, *Phys. Earth Planet. Int.*, *112*, 211–256.
Walzer, U., R. Hendel, and J. Baumgardner (2004a), The effects of a variation of the radial viscosity profile on mantle evolution, *Tectonophysics*, *384*, 55–90.
Walzer, U., R. Hendel, and J. Baumgardner (2004b), Toward a thermochemical model of the evolution of the Earth's mantle, in *High Perf. Comp. Sci. Engng. '04*, edited by E. Krause, W. Jäger, and M. Resch, pp. 395–454, Springer, Berlin.
Wedepohl, K. H. (1995), The composition of the continental crust, *Geochim. Cosmochim. Acta*, *59*, 1217–1232.
Willbold, M., and A. Stracke (2006), Trace element composition of mantle end-members: Implications for recycling of oceanic and upper and lower continental crust, *Geochem. Geophys. Geosyst.*, *7*, Q04004, doi:10.1029/2005GC001005.
Windley, B. F. (1995), *The Evolving Continents*, 526 pp., Wiley, Chichester.
Yamazaki, D., and S.-I. Karato (2001), Some mineral physics constraints on the rheology and geothermal structure of the Earth's lower mantle, *Am. Miner.*, *86*, 385–391.
Yang, W.-S. (1997), Variable viscosity thermal convection at infinite prandtl number in a thick spherical shell, Ph.D. thesis, Univ. of Illinois, Urbana-Champaign, Ill.
Zhong, S., and M. Gurnis (1993), Dynamic feedback between a continent-like raft and thermal convection, *J. Geophys. Res.*, *98*, 12,219–12,232.
Zhong, S., N. Zhang, Z.-X. Li, and J. H. Roberts (2007), Supercontinental cycles, true polar wander, and very long-wavelength mantle convection, *Earth Planet. Sci. Lett.*, *261*, 551–564.

R. Hendel and U. Walzer, Institut f. Geowissenschaften, Friedrich-Schiller-Universität, Burgweg 11, 07749 Jena, Germany. (u.walzer@uni-jena.de)

accepted for publication in JOURNAL OF GEOPHYSICAL RESEARCH , 6 May 2008